A&A 594, A28 (2016)
DOI: 10.1051/0004-6361/201525819

Astronomy & Astrophysics
Special feature

Planck 2015 results

Planck 2015 results

XXVIII. The *Planck* Catalogue of Galactic cold clumps

Planck Collaboration: P. A. R. Ade[85], N. Aghanim[60], M. Arnaud[73], M. Ashdown[69,5], J. Aumont[60], C. Baccigalupi[84], A. J. Banday[94,8], R. B. Barreiro[65], N. Bartolo[29,66], E. Battaner[96,97], K. Benabed[61,93], A. Benoît[58], A. Benoit-Lévy[23,61,93], J.-P. Bernard[94,8], M. Bersanelli[32,49], P. Bielewicz[94,8,84], A. Bonaldi[68], L. Bonavera[65], J. R. Bond[7], J. Borrill[13,89], F. R. Bouchet[61,87], F. Boulanger[60], M. Bucher[1], C. Burigana[48,30,50], R. C. Butler[48], E. Calabrese[91], A. Catalano[74,72], A. Chamballu[73,15,60], H. C. Chiang[26,6], P. R. Christensen[81,36], D. L. Clements[56], S. Colombi[61,93], L. P. L. Colombo[22,67], C. Combet[74], F. Couchot[70], A. Coulais[72], B. P. Crill[67,10], A. Curto[5,65], F. Cuttaia[48], L. Danese[84], R. D. Davies[68], R. J. Davis[68], P. de Bernardis[31], A. de Rosa[48], G. de Zotti[45,84], J. Delabrouille[1], F.-X. Désert[54], C. Dickinson[68], J. M. Diego[65], H. Dole[60,59], S. Donzelli[49], O. Doré[67,10], M. Douspis[60], A. Ducout[61,56], X. Dupac[38], G. Efstathiou[62], F. Elsner[23,61,93], T. A. Enßlin[78], H. K. Eriksen[63], E. Falgarone[72], J. Fergusson[11], F. Finelli[48,50], O. Forni[94,8], M. Frailis[47], A. A. Fraisse[26], E. Franceschi[48], A. Frejsel[81], S. Galeotta[47], S. Galli[61], K. Ganga[1], M. Giard[94,8], Y. Giraud-Héraud[1], E. Gjerløw[63], J. González-Nuevo[65,84], K. M. Górski[67,98], S. Gratton[69,62], A. Gregorio[33,47,53], A. Gruppuso[48], J. E. Gudmundsson[26], F. K. Hansen[63], D. Hanson[79,67,7], D. L. Harrison[62,69], G. Helou[10], S. Henrot-Versillé[70], C. Hernández-Monteagudo[12,78], D. Herranz[65], S. R. Hildebrandt[67,10], E. Hivon[61,93], M. Hobson[5], W. A. Holmes[67], A. Hornstrup[16], W. Hovest[78], K. M. Huffenberger[24], G. Hurier[60], A. H. Jaffe[56], T. R. Jaffe[94,8], W. C. Jones[26], M. Juvela[25], E. Keihänen[25], R. Keskitalo[13], T. S. Kisner[76], J. Knoche[78], M. Kunz[17,60,2], H. Kurki-Suonio[25,43], G. Lagache[4,60], J.-M. Lamarre[72], A. Lasenby[5,69], M. Lattanzi[30], C. R. Lawrence[67], R. Leonardi[38], J. Lesgourgues[92,83,71], F. Levrier[72], M. Liguori[29,66], P. B. Lilje[63], M. Linden-Vørnle[16], M. López-Caniego[38,65], P. M. Lubin[27], J. F. Macías-Pérez[74], G. Maggio[47], D. Maino[32,49], N. Mandolesi[48,30], A. Mangilli[60,70], D. J. Marshall[73], P. G. Martin[7], E. Martínez-González[65], S. Masi[31], S. Matarrese[29,66,41], P. Mazzotta[34], P. McGehee[57], A. Melchiorri[31,51], L. Mendes[38], A. Mennella[32,49], M. Migliaccio[62,69], S. Mitra[55,67], M.-A. Miville-Deschênes[60,7], A. Moneti[61], L. Montier[94,8,⋆], G. Morgante[48], D. Mortlock[56], A. Moss[86], D. Munshi[85], J. A. Murphy[80], P. Naselsky[81,36], F. Nati[26], P. Natoli[30,3,48], C. B. Netterfield[19], H. U. Nørgaard-Nielsen[16], F. Noviello[68], D. Novikov[77], I. Novikov[81,77], C. A. Oxborrow[16], F. Paci[84], L. Pagano[31,51], F. Pajot[60], R. Paladini[57], D. Paoletti[48,50], F. Pasian[47], G. Patanchon[1], T. J. Pearson[10,57], V.-M. Pelkonen[57], O. Perdereau[70], L. Perotto[74], F. Perrotta[84], V. Pettorino[42], F. Piacentini[31], M. Piat[1], E. Pierpaoli[22], D. Pietrobon[67], S. Plaszczynski[70], E. Pointecouteau[94,8], G. Polenta[3,46], G. W. Pratt[73], G. Prézeau[10,67], S. Prunet[61,93], J.-L. Puget[60], J. P. Rachen[20,78], W. T. Reach[95], R. Rebolo[64,14,37], M. Reinecke[78], M. Remazeilles[68,60,1], C. Renault[74], A. Renzi[35,52], I. Ristorcelli[94,8], G. Rocha[67,10], C. Rosset[1], M. Rossetti[32,49], G. Roudier[1,72,67], J. A. Rubiño-Martín[64,37], B. Rusholme[57], M. Sandri[48], D. Santos[74], M. Savelainen[25,43], G. Savini[82], D. Scott[21], M. D. Seiffert[67,10], E. P. S. Shellard[11], L. D. Spencer[85], V. Stolyarov[5,69,90], R. Sudiwala[85], R. Sunyaev[78,88], D. Sutton[62,69], A.-S. Suur-Uski[25,43], J.-F. Sygnet[61], J. A. Tauber[39], L. Terenzi[40,48], L. Toffolatti[18,65,48], M. Tomasi[32,49], M. Tristram[70], M. Tucci[17], J. Tuovinen[9], G. Umana[44], L. Valenziano[48], J. Valiviita[25,43], B. Van Tent[75], P. Vielva[65], F. Villa[48], L. A. Wade[67], B. D. Wandelt[61,93,28], I. K. Wehus[67], D. Yvon[15], A. Zacchei[47], and A. Zonca[27]

(Affiliations can be found after the references)

Received 5 February 2015 / Accepted 16 August 2015

ABSTRACT

We present the *Planck* Catalogue of Galactic Cold Clumps (PGCC), an all-sky catalogue of Galactic cold clump candidates detected by *Planck*. This catalogue is the full version of the Early Cold Core (ECC) catalogue, which was made available in 2011 with the Early Release Compact Source Catalogue (ERCSC) and which contained 915 high signal-to-noise sources. It is based on the *Planck* 48-month mission data that are currently being released to the astronomical community. The PGCC catalogue is an observational catalogue consisting exclusively of Galactic cold sources. The three highest Planck bands (857, 454, and 353 GHz) have been combined with IRAS data at 3 THz to perform a multi-frequency detection of sources colder than their local environment. After rejection of possible extragalactic contaminants, the PGCC catalogue contains 13188 Galactic sources spread across the whole sky, i.e., from the Galactic plane to high latitudes, following the spatial distribution of the main molecular cloud complexes. The median temperature of PGCC sources lies between 13 and 14.5 K, depending on the quality of the flux density measurements, with a temperature ranging from 5.8 to 20 K after removing the sources with the top 1% highest temperature estimates. Using seven independent methods, reliable distance estimates have been obtained for 5574 sources, which allows us to derive their physical properties such as their mass, physical size, mean density, and luminosity. The PGCC sources are located mainly in the solar neighbourhood, but also up to a distance of 10.5 kpc in the direction of the Galactic centre, and range from low-mass cores to large molecular clouds. Because of this diversity and because the PGCC catalogue contains sources in very different environments, the catalogue is useful for investigating the evolution from molecular clouds to cores. Finally, it also includes 54 additional sources located in the Small and Large Magellanic Clouds.

Key words. ISM: clouds – ISM: structure – local insterstellar matter – stars: formation

⋆ Corresponding author: Ludovic Montier, e-mail: Ludovic.Montier@irap.omp.eu

1. Introduction

The all-sky *Planck*[1] mission has opened up the possibility of carrying out comprehensive investigations of the Galactic emission components. With its high sensitivity and wide wavelength coverage, *Planck* provides all-sky maps of the thermal dust emission and, in particular, of the emission arising from cold dust. Because cold dust is mainly associated with dense regions within molecular clouds, these observations are relevant for studies of the early phases of star formation, in particular to explore how star formation depends on the physical conditions provided by the parent cloud. To this end, it is necessary to investigate the spatial distribution and physical properties of dense clumps in different Galactic environments, and this objective can be attained only by extended surveys, which can cover the full range of scales encompassed by the star formation process, i.e., from subparsec to several kpc.

During the past decade, new insights into the study of cold sources have been provided by sophisticated numerical modelling and by the development of sensitive millimetre and submillimetre detectors, operating both from space and from the ground, and with either imaging or spectroscopic capabilities (e.g., Sect. 1 in Planck Collaboration XXIII 2011). By combining the highest frequency channels of the *Planck* survey (353−857 GHz, 850−350 μm) with the far-infrared IRAS (Neugebauer et al. 1984) data, and by applying a dedicated source detection method, which leverages on the spectral signature of cold sources, we can obtain an all-sky census of the coldest Galactic objects. In particular, the method of Montier et al. (2010) makes it possible to separate cold and warm dust emission components, and to derive the physical properties (flux density, size of the emitting region, temperature) of the cold component. Furthermore, *Planck* has provided the first uniform submillimetre surveys that cover both the Galactic plane and regions at intermediate and high latitudes, which allows us to expand the physical parameter space probed by the previously known cold sources. The *Planck* detected sources span a broad range of temperature, mean density, mass, and size. The most compact and nearby sources have a linear diameter of ∼0.1 pc. At large distances, though, and because of the limited instrument resolution, many sources have an intrinsic size of tens of parsec. More importantly, the average *Planck* cold clump, with a linear diameter of 1 pc, is typically characterized by the presence of substructures, each corresponding to individual cores, as revealed by the *Herschel* follow-up (Juvela et al. 2010, 2011, 2012; Planck Collaboration XXII 2011; Montillaud et al. 2015). The *Herschel* observations also highlighted that the *Planck* sources likely correspond to different evolutionary stages, with half of the targeted fields showing signs of active star formation, as indicated by the presence of mid-infrared point sources. In addition, the *Herschel* high-angular resolution has allowed us to shed light on the filamentary nature of a substantial fraction of *Planck* clumps and has shown, in one case out of ten, that the clumps have a cometary shape or a sharp boundary indicative of compression by an external force (Juvela et al. 2012).

As part of the first *Planck* data release, the sample of the most robust *Planck* detections has already been delivered to the astronomical community. This Early Cold Clump sample (ECC) included 915 *Planck* cold clumps (at $T < 14$ K) that are distributed over the whole sky (Planck Collaboration VII 2011; Planck Collaboration 2011). We are now providing the entire catalogue of cold sources, i.e., the Planck Catalogue of Galactic Cold Clumps (PGCC), based on the full *Planck* 2014 data release over the whole sky and shown in Fig. 1.

In this paper, we describe the generation and content of the PGCC catalogue. A detailed analysis of the cold source population contained in the catalogue will be presented in forthcoming papers. In Sect. 2 we describe the data as well as the source detection and extraction method. In Sect. 3 we discuss the generation of the catalogue, including the applied quality flags for the source selection and the photometric measurements. In Sect. 4 we discuss the source validation process of the detection algorithm, based on a statistical analysis. In Sect. 5 we present the different methods used to derive distance estimates for the clumps. In Sect. 6 we describe the derivation of other physical properties of the sources such as mass and luminosity. Finally, in Sect. 7, we provide details on the cross-matching of the final catalogue with ancillary catalogues and complementary data sets.

2. Source detection and photometry

2.1. Data set

This paper is based on the whole observing time of the *Planck* mission, corresponding to the 5 all-sky surveys. Here we approximate the *Planck* beams by using effective circular Gaussians (Planck Collaboration IV 2014; Planck Collaboration VI 2014). The full-width-half-maximum (FWHM) at each frequency channel is given in Table 1. In addition, in this work, we focus on the three highest *Planck* frequency channels, i.e., 857, 545, and 353 GHz, which are designed to cover the Galactic cold dust emission peak. The 217 GHz band has not been included in our analysis, although it is characterized by an angular resolution comparable to the other bands, and this is for two reasons: i) this band is strongly contaminated by the CO $J = 2 \rightarrow 1$ emission line, as described in Planck Collaboration IX (2014), and this contribution is expected to be significant towards dense regions, given their associations with molecular material; ii) the contamination by the cosmic microwave background may become problematic in this band at high latitude, implying a complex component separation issue. The noise in the channel maps is assumed to be Gaussian with a standard deviation of 1.55×10^{-2}, 1.49×10^{-2} and 1.4×10^{-3} MJy sr^{-1} at 857, 545, and 353 GHz, respectively (Planck Collaboration I 2014). The absolute gain calibration of High Frequency Instrument (HFI) maps is about 1.2%, 6.08%, and 6.33% at 353, 545, and 857 GHz, respectively (see Table 6 in Planck Collaboration I 2014). Further details on the data reduction, *Planck* frequency maps and the calibration scheme can be found in Planck Collaboration VI (2014).

The *Planck* data are combined with the IRIS all-sky data (Miville-Deschênes & Lagache 2005), i.e., a reprocessed version of the IRAS data. As described in Planck Collaboration VII (2011) and Planck Collaboration XXIII (2011), the IRIS 3 THz (100 μm) data have been chosen because they allow us to complement the *Planck* data. In fact: i) 3 THz is a very good tracer of Galactic warm (∼20 K) dust; ii) the emission from small grains does not contribute substantially at this frequency; iii) the IRIS (4.′3) and *Planck* data angular resolutions are very similar (see Table 1). We note that the IRAS survey coverage presents two gaps, which in total account for 2% of the whole sky. In

[1] *Planck* (http://www.esa.int/Planck) is a project of the European Space Agency (ESA) with instruments provided by two scientific consortia funded by ESA member states and led by Principal Investigators from France and Italy, telescope reflectors provided through a collaboration between ESA and a scientific consortium led and funded by Denmark, and additional contributions from NASA (USA).

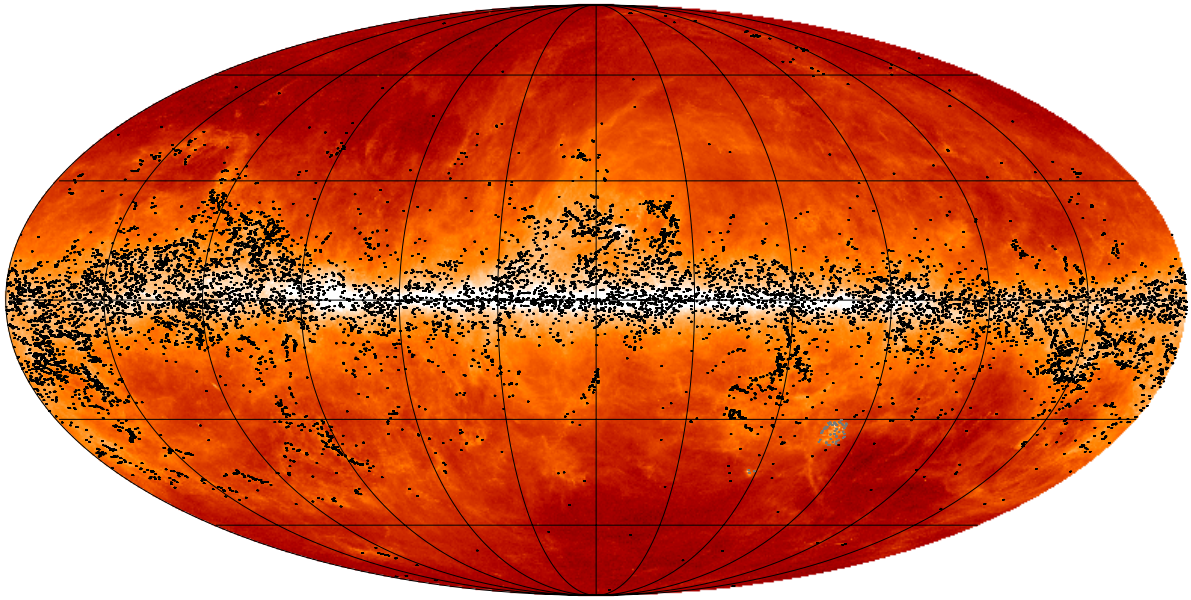

Fig. 1. All-sky distribution of the PGCC sources: 13188 Galactic clumps (black dots), plus 54 Large Magellanic Cloud (LMC) and Small Magellanic Cloud (SMC) clumps (grey dots). The source distribution is overlaid on the 857 GHz *Planck* map, shown in logarithmic scale between 10^{-2} to 10^{2} MJy sr^{-1}.

Table 1. FWHM of the effective beam of the IRAS and *Planck* high frequency channel maps.

Frequency [GHz]	Wavelength [μm]	*FWHM* [′]
353	850	4.818 ± 0.024
545	550	4.682 ± 0.044
857	350	4.325 ± 0.055
3000	100	4.300 ± 0.200

IRIS data, these gaps were filled in by using lower angular resolution *DIRBE* data (∼40′). Because of the discrepancy in resolution between IRIS and *DIRBE*, these regions have been excluded from our analysis. Furthermore, sources detected by our algorithm close to the location of the gaps were carefully examined, since they might be contaminated by noisy features in the IRIS 3 THz map.

All *Planck* and IRIS maps have been convolved to the same resolution, 5′ FWHM, before performing source detection and extraction.

2.2. Detection method

To detect cold sources in the combined *Planck* and IRIS 3 THz maps, we applied the CoCoCoDeT detection algorithm presented in Planck Collaboration XXIII (2011), and described in Montier et al. (2010). This algorithm is based on a multi-frequency approach which exploits the specific colour properties of this type of sources. The detection is performed independently at 857, 545, and 353 GHz using the cold residual maps, which are built by subtracting a warm component from each frequency map. This warm component is estimated separately in each pixel by extrapolating a warm template, i.e., the IRIS 3 THz map, to a given *Planck* frequency ν, using the local average background colour estimated at 3 THz and ν, and computed in an annulus from 5′ to 15′ centred on the pixel. The catalogues obtained in each of the three *Planck* bands, 857, 545, and 353 GHz, are then merged by requiring: i) a detection in each band on the cold residual maps; ii) a signal-to-noise ratio (S/N) greater than 4 in all bands; iii) a maximum distance between the centres of the three detections of 5′. These criteria ensure cross-band detection consistency as well as source compactness. More details can be found in Planck Collaboration XXIII (2011).

We emphasize that our method differs from classical detection algorithms that typically perform the detection directly on frequency maps, as for instance is the case for the Planck Catalogue of Compact Sources (PCCS, Planck Collaboration XXVIII 2014). Our method allows a detection in *temperature*: cold sources show a positive signal in the cold residual maps, while warm sources show a negative signal. More precisely, this technique allows us to enhance sources having a temperature lower than the local background. This does not automatically imply that the detected sources are intrinsically cold: for example, a source could be detected as *cold* simply because it is seen against a very warm background (or foreground). This is the typical case of objects located along the line-of-sight of active star forming regions. In building the catalogue, this effect has been taken into account, as discussed in Sect. 3.4.

2.3. Photometry

The flux density of the cold clumps has been estimated from the IRIS and *Planck* bands using the algorithm described in Planck Collaboration XXIII (2011). Here we recall the main steps of the method: i) determination of the clump size and position by means of an elliptical Gaussian fit of the 857 GHz over 3 THz colour ratio map at the location where the S/N is the highest; ii) polynomial fit of the background surface at 3 THz and removal of the cold component from the 3 THz warm template before extrapolation to the *Planck* bands; iii) aperture photometry in all bands using the elliptical profile. We provide two estimates of the flux density in each band, one for the cold clump and one for its associated warm background. The estimate for the clump is based on the cold residual maps, after subtraction of the warm component, while the warm background flux density is

computed from the warm component, extrapolated from 3 THz and integrated over a solid angle with the same size as the cold clump. The sum of these two values gives the total flux density of the cold clump in the original IRIS and *Planck* maps. We stress that the cold residual maps used to compute the aperture photometry are the one obtained after subtracting the cold clump component from the warm template at 3 THz.

The uncertainty on the flux density estimates have been obtained by performing Monte Carlo simulations. In particular, for each source we inject one at a time, in an annulus extending from 10′ to 30′ centred on the source itself and in both the IRIS and *Planck* cold residual maps, artificial sources with the same flux density and elliptical shape. This operation allows us to preserve the instrumental noise and confusion level of the original maps. The uncertainty on the true source photometric measurement is then given by the standard deviation of the flux densities of the artificial sources when the same photometric steps are applied to both the true and artificial sources. We emphasize that our flux density uncertainties are likely slightly conservative, as the confusion arising from injecting artificial sources in the proximity of the true source generates additional noise and this term is included in our calculations. More details can be found in Planck Collaboration XXIII (2011). We have performed a Monte Carlo quality assessment (MCQA) to evaluate the overall quality of our photometric measurements and this is presented in Sect. 4. As in Planck Collaboration XXIII (2011), we assign to the catalogued sources quality flags to indicate the accuracy on the estimated flux densities and sizes, and these flags are used to divide the sources into three categories of increasing flux quality, as described in Sect. 3.1.

We note that a minimum distance of 5′ between two sources was required for detections at 857, 545, and 353 GHz. However, band-merging and elliptical Gaussian fitting both modify the final centroid coordinates of the clumps, which therefore may not longer satisfy the 5′ criterion. Furthermore, elongated clumps may partially overlap even at a distance greater than 5′ between them. Because Galactic very sources are preferentially found highly structured regions of the Galaxy, where confusion is significant, we have to face severe blending issues. After obtaining the elliptical Gaussian profile of all the sources, we compute the overlap between a given source and all its neighbours located within 15′. All sources with a non-zero overlap are flagged (`FLUX_BLENDING`), and further information is provided, as detailed in Sect. 3.2.

3. Catalogue generation

In this section, we describe the final selection of sources, starting from the source list generated by the detection algorithm. In particular, we discuss how we have increased the reliability of the catalogue by rejecting spurious sources and extragalactic contaminants. Finally, we provide details on the catalogue content.

3.1. Selection based on photometric quality

We have seen that the detection algorithm described in Sect. 2.2 has been applied to the combined *Planck* and IRIS 3 THz data. After rejection of the spurious detections obtained in the proximity of the gaps in the IRAS map, we are left with 13 832 sources. As a first validation step, we have used the quality of the photometric measurements discussed in Sect. 2.3 to identify additional spurious sources. Following this procedure, 428 detections (∼3% of the total) are rejected because of highly inaccurate photometry. The typical case of rejected sources at this stage is that of sources with a negative flux density estimate, which can be caused by the presence of stripes in the data. The 13 404 remaining sources have been divided into three categories, according to the quality of their flux density values (see `FLUX_QUALITY` flag). The three categories are:

Table 2. Description of the PGCC content, providing the total number of initial, rejected, final and flagged sources, and split in each category of the flux density quality.

	`FLUX_QUALITY` 1	2	3	Total
Initial	7062	3833	2509	13404
Extragalactic sources	46	40	28	114
LMC/SMC	19	25	10	54
Nearby hot sources	4	13	31	48
Final	6993	3755	2440	13188
Flag nearby hot sources	758	1025	633	2416
Flag blending	726	528	503	1757
With distance estimate	2940	1686	948	5574

category 1: "*Reliable flux densities*": sources with flux densities at $S/N > 1$ in both *Planck* (857, 545, and 353 GHz) and IRIS 3 THz bands, allowing a full characterization of their colour ratio and their temperature, as required for their validation. These sources represent the highest quality sample of the PGCC catalogue, and have `FLUX_QUALITY`=1.

category 2: "*Missing 3 THz flux density*": sources with flux densities $S/N > 1$ in all bands except for the IRIS 3 THz band, where we have obtained only an upper limit. These sources are typically characterized by low flux densities and extremely cold temperatures, and have no detectable counterparts in the infrared. They are potentially interesting very cold clump candidates, and have `FLUX_QUALITY`=2.

category 3: "*Detection only*": sources for which the quality of the elliptical Gaussian fit is very poor, thus no reliable flux density estimate can be obtained. These sources are likely extended or embedded in a complex environment. They have `FLUX_QUALITY`=3.

We provide the number of sources in each category in the first row of Table 2. After removal of the contaminants, such as sources affected by the presence of nearby hot sources (see Sect. 3.4) or extragalactic objects (see Sect. 3.3), we obtain the final number of sources shown in the last row of the Table. The all-sky distributions of the sources in each `FLUX_QUALITY` (hereafter FQ) category are shown in Fig. 2.

3.2. Blending issue

A total of 1757 sources are affected by blending, i.e., their flux density estimates have been compromized by the presence of a nearby and partly overlapping source. In this case, the flag `FLUX_BLENDING` is raised, and an approximate estimation of the contamination level is performed. This is expressed in terms of a relative bias (`FLUX_BLENDING_BIAS`) of the original flux density estimate in each band, when flux density estimates are available for both involved sources. The median value of this bias is around −37%, although it varies greatly from one source to another. This bias is only indicative and cannot be used to correct the flux density estimates. A more accurate estimate of these flux densities could be obtained by performing a detailed analysis on individual sources, which, in particular, should take into account

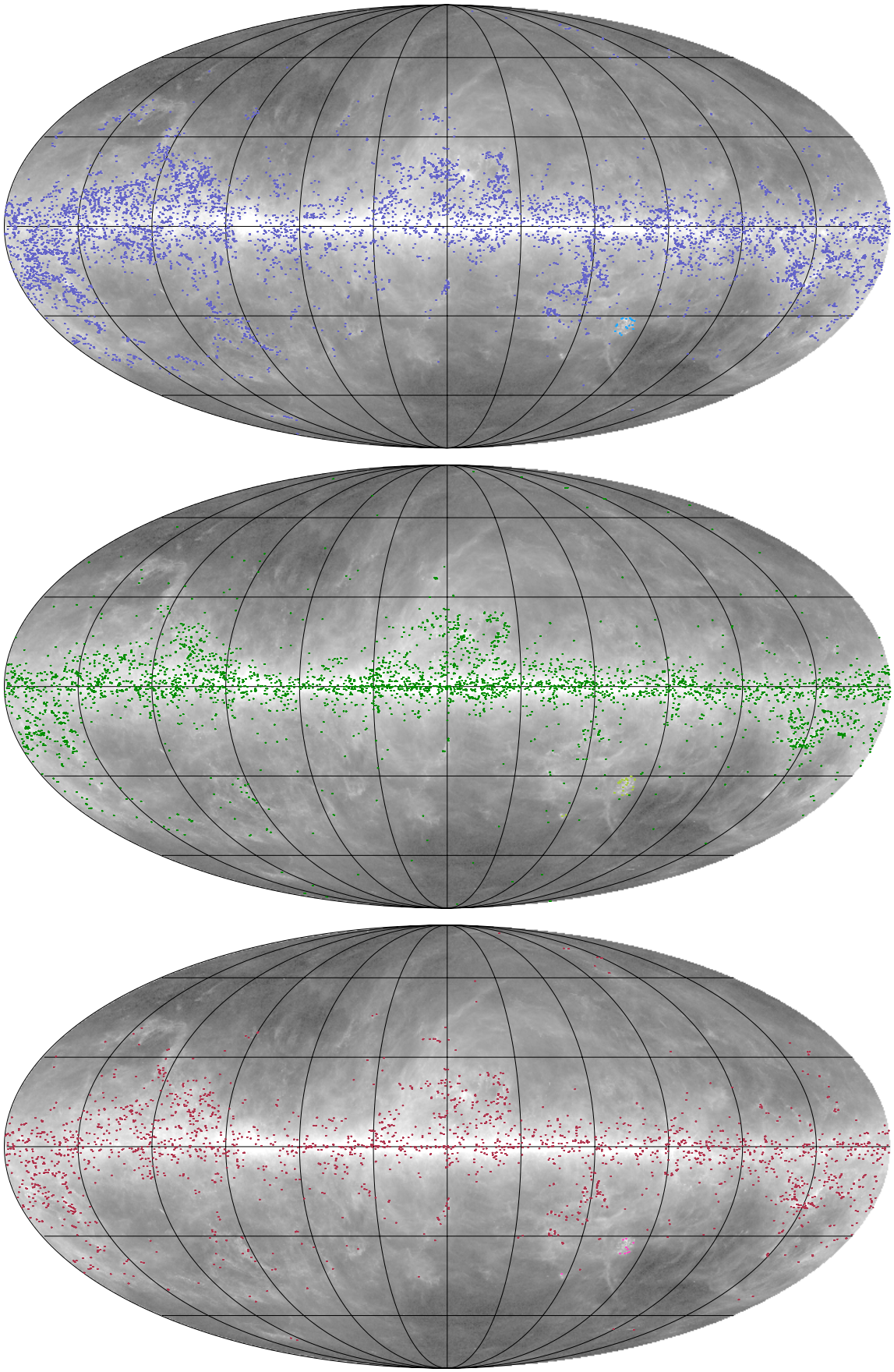

Fig. 2. All-sky distribution of the PGCC sources according to their `FLUX_QUALITY` category: "Reliable flux densities" (FQ = 1, *top panel*), "Missing 3 THz flux density" (FQ = 2, *middle panel*) and "Detection only" (FQ = 3, *bottom panel*). Sources located in the LMC and SMC are also shown in light colours.

the local background fluctuations, hence the relative contribution of each source component to the integrated flux density. A visual inspection to the ID cards of the blended sources may help to get an idea of the complexity of each case. For each source impacted by blending, we also provide the catalogue index of the companion source (FLUX_BLENDING_IDX) with the angular distance to its centroid (FLUX_BLENDING_ANG_DIST).

3.3. Extragalactic contamination

The goal of the PGCC catalogue is to contain a selection as large as possible of Galactic cold clump candidates. Since the CoCoCoDeT detection algorithm is applied to all-sky maps, it is possible to have contamination from extragalactic objects. Hereafter we describe the three independent methods that we have used to identify and reject this type of contaminants.

The first step consists of a colour-colour selection of "radio-type" objects, characterized by a flat spectral energy distribution (SED) in the submillimetre and millimetre wavelength range. This kind of objects may have been detected by our algorithm because of the flattening of their SED around 857 and 545 GHz, which tends to mimic a cold black body spectrum. In this case, we have used the 353 GHz to 545 GHz flux density ratio to discriminate between radio-emitting and other type of objects. We found 26 objects with a ratio $S_{353}/S_{545} > 0.9$, typical of an extremely flat or increasing SED in the millimetre domain.

The second step consists in cross-correlating the PGCC catalogue with extragalactic catalogues, such as: the Messier (Messier & Niles 1981) catalogue, the NGC (Dreyer 1888) and IC (Dreyer 1895) catalogues of nearby galaxies, and the 3C (Edge et al. 1959; Bennett 1962) and 4C (Pilkington & Scott 1965; Gower et al. 1967) catalogues of quasars. The cross-correlation has been performed using a 5′ radius, leading to 66 found associations between a cold clump and an extragalactic object.

In the last step, we have searched for possible optical counterparts in the Digitized Sky Survey (DSS) data (Djorgovski et al. 2003). The whole sample of cold clump candidates has been visually inspected to look for extended and/or bright sources in DSS images located close to or at the cold clump coordinates. After selecting some 800 sources with potential DSS counterparts, for each of these we have carefully examined ancillary Dame et al. (2001) CO data, extinction maps obtained with the NICER algorithm (Lombardi 2009) and cold residual maps. In addition, we have also searched for possible counterparts in the *Planck* Low Frequency Instrument (LFI) data. The combination of all these data sets has allowed us to identify 43 sources that are likely of extragalactic origin.

Finally, we have merged the three samples of extragalactic contaminants and rejected 114 unique objects from the initial source list.

The CoCoCoDeT algorithm has also detected sources in the Large Magellanic Cloud (LMC) and the Small Magellanic Cloud (SMC), which have not been rejected from the catalogue. Because of the proximity of these two galaxies, the *Planck* resolution and sensitivity allow the detection of individual cold clumps, forming a potential very interesting sample. Hence 51 *Planck* clumps falling inside a radius of 4.°09 centred on the Galactic coordinates (279.03, −33.60), as defined by Staveley-Smith et al. (2003), are flagged (XFLAG_LMC) as part of the LMC, and 3 others falling inside a radius of 2.°38 centred on the Galactic coordinates (302.67, −44.46), following Stanimirovic et al. (1999), are flagged (XFLAG_SMC) as part of the SMC. Remarkably, follow-up observations of the LMC and SMC *Planck* clump candidates have confirmed the nature of these objects, as discussed in Appendix A.

3.4. Nearby hot source contamination

The detection algorithm CoCoCoDeT (Montier et al. 2010) used to extract the cold clumps from the *Planck* and IRIS data is designed to detect sources colder than a median background estimated in the neighbourhood of the source. As stressed in Sect. 2.2, this method allows us to detect cold regions embedded in a warm background, but it can also yield detections of extended envelopes of warm sources that appear colder than their environment but are not intrinsically cold. In some extreme cases, a hot source can cause an overestimation of the background temperature in its proximity and thus lead to spurious detections.

In order to investigate this type of contamination, we use the cold residual maps as an indicator of the warm background around the source and look for negative contiguous pixels. By definition, where the cold residual is positive, the relative temperature is colder than the background, and the other way round, i.e., where the residual is negative, the temperature is higher. Thus we can build a list of hot point sources by using the same detection algorithm as for the cold clumps, but this time by applying it to the reverse of the cold residual maps. We then compute the minimum distance between any cold clump candidate and hot source detections in a 15′ radius from the cold clump coordinates centre. This yields 2464 cold-hot associations with distances ranging from 2.′6 to 15′.

We emphasize that the presence of hot sources in the proximity of cold sources does not lead systematically to spurious detections. This kind of association is expected in star formation regions, as both pre- and proto-stellar cores often reside in the same molecular cloud. In fact, the formation of cold and compact condensations may even be triggered by nearby star formation. For this reason, we only reject cold clump detections that are associated with a hot source located inside a 5′ radius from the cold clump coordinate centre (48 sources) and we flag the other 2416 cases while providing the distance between the centre of the cold clump and the hot source (NEARBY_HOT_SOURCE).

3.5. Description of the catalogue content

The final PGCC catalogue counts 13 188 Galactic sources and 54 sources located in the LMC and SMC, divided into three categories of flux density quality (FLUX_QUALITY flag). The number of sources in each category is given in Table 2. The table also provides the number of sources that are flagged due to the presence of nearby hot sources (NEARBY_HOT_SOURCE flag) or because they are located in the LMC and SMC. The all-sky distribution of the PGCC sources, shown in Fig. 1, globally follows the main molecular structures of the Galaxy, as illustrated by comparing with the *Planck* all-sky CO map in Fig. B.1. The all-sky distribution of the PGCC for each flux density quality category is shown in Fig. 2. The latitude distribution, presented in Fig. 3, shows that the FQ = 2 (coldest candidates) sources are preferentially detected towards the Galactic plane, compared to the FQ = 1 (highest reliability) sources that exhibit a deficit of sources in the Galactic plane. The same effect is observed for the FQ = 3 (detection only) sources, which may be explained by the confusion in those regions.

The columns in the catalogue and their meaning is given in Tables C.1. The distance estimates and related physical

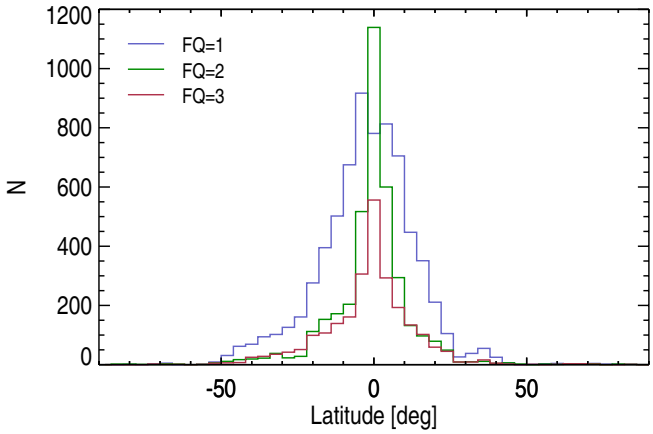

Fig. 3. Distribution of the PGCC sources as a function of the latitude for each FLUX_QUALITY category.

properties are described in Sects. 5 and 6. The PGCC catalogue is available online on the Planck Legacy Archive[2] and on the MuFFInS[3] (Multi Frequency Follow-up Inventory Service) portal, together with 30′ × 30′ cutouts, respectively, from the IRIS 3 THz, the *Planck* frequency map, and the *Planck* cold residual maps.

4. Quality assessment

4.1. MCQA simulations

We have carried out a MCQA to quantify the performance of the detection algorithm applied to the combined IRIS 3 THz and *Planck* data set. To this end, we have generated all-sky simulations by injecting artificial sources in the IRIS and *Planck* maps, and then applied the CoCoCoDeT algorithm described in Sect. 2.2. In total, 150 000 sources have been injected over the whole sky, divided into 15 sky realizations. Each source is characterized by a temperature, a fixed emissivity spectral index $\beta = 2$, a flux density at 857 GHz, and an elliptical Gaussian profile (major and minor axis, ellipticity and position angle). The simulated sources are randomly distributed across the sky, using a uniform spatial distribution, at a minimum distance of 12′ from the true *Planck* cold clump centre coordinates.

The synthetic temperatures range from 6 to 20 K, while the synthetic flux densities at 857 GHz follow a uniform distribution in logarithmic scale between 1.5 Jy and 500 Jy, indicating that we inject more faint sources that are effectively detected. Temperatures and flux densities are independently assigned to a value, i.e., no functional relation is assumed between these two quantities. The ellipticity varies between 1 and 2, and θ ranges from 5′ to 7′.

We note that these simulations do not intend to accurately reproduce the *Planck* cold clump properties. Their goal is rather to cover entirely the physically acceptable parameter space, in order to allow us to recover the CoCoCoDeT transfer function.

The detection and extraction procedure, described in Sects. 2.2 and 2.3, is then applied to the simulated data set, and a catalogue of detected sources, with corresponding flux densities and FLUX_QUALITY flag, is built.

[2] PLA: http://www.cosmos.esa.int/web/planck/pla
[3] MuFFInS: http://muffins.irap.omp.eu

4.2. Completeness

Completeness is defined as the ratio of the number of detected sources to the total number of injected sources. Using the Monte Carlo analysis described in the previous section, we have investigated whether the completeness of the catalogue generated with the CoCoCoDeT algorithm depends on temperature, Galactic latitude, flux density and mass.

The top panel of Fig. 4 shows the relation between catalogue completeness and temperature of the injected sources. The total completeness (when including sources with all FLUX_QUALITY category) is about 80% for input temperatures lower than 10 K, while it drops below 1% for temperatures larger than 17 K. In addition, the total completeness increases to almost 90%, for temperatures below 10 K if we consider only sources with input flux densities $S_{857} > 15$ Jy (dotted line). This result confirms that CoCoCoDeT is a method optimized to detect cold sources embedded in a warm environment, while rejecting warm sources. We also note that sources flagged with FQ = 3, (i.e., *Detection only*) are found in correspondence of relatively warm temperatures (between 12 and 18 K), indicating that, as discussed in Sect. 3.1, they might not be cold clumps. On the other hand, the completeness of the sources with FQ = 2 (i.e., *Missing 3 THz flux*) increases towards lower temperatures, further suggesting that they are probably very cold. The anti-correlation between the trends of the completeness of sources with FQ = 2 (increasing) and with FQ = 1 (decreasing) below 10 K, is clearly due to the lack of sensitivity of the IRIS 3 THz data. Cold sources will be barely detectable in the IRIS 3 THz band and mostly classified in the FQ = 2 category. We note that the completeness of sources with very low temperature (close to 6 K) is still about 60%, which means that, if these sources indeed exist, our algorithm is able to detect them. Finally, the completeness of the most reliable set of sources (FQ = 1, blue) appears to peak (at 40%) around 12 K, ranging from 17 K to 6 K, i.e., the floor of the temperature distribution of the injected sources. Because the detection efficiency drops to zero beyond 17 K, in the following we limit the discussion to simulated sources with temperatures lower than this threshold.

The middle panel of Fig. 4 illustrates the completeness as a function of Galactic latitude. Outside the Galactic plane, the completeness cumulated over all FQ categories remains quite constant and around 60%, while it drops to 30% for $|b| < 10°$. This effect is expected and due to confusion in the Galactic plane. Sources with FQ = 1 and 2 present a similar behaviour. On the contrary, the simulated sources with FQ = 3 are mainly detected outside the plane, as observed for the real PGCC sources in this flux category (see bottom panel of Fig. 2).

We have also explored the dependence of the completeness on the injected flux density in the IRIS 3 THz and *Planck* bands. The result is in Fig. 5. The completeness of the FQ = 3 sources increases with flux density, especially at the two highest frequencies. This is indeed the behaviour we expect from relatively warm sources. Conversely, the completeness of the FQ = 2 sources, which are presumably very cold, peaks at bright flux densities in the two lower frequencies, and at faint flux densities (below 1 Jy) at 3 THz, where it has not been possible to get any output flux density estimates. The completeness at 3 THz of the FQ = 1 sources that, by definition, have $S/N > 1$, is about 20% below the IRIS sensitivity limit (1 Jy), and may appear inconsistent with it. This comes from the fact that completeness in a given band is here defined based on the input source flux density rather than on the output one. If we estimate the completeness by using only the sources for which the recovered flux

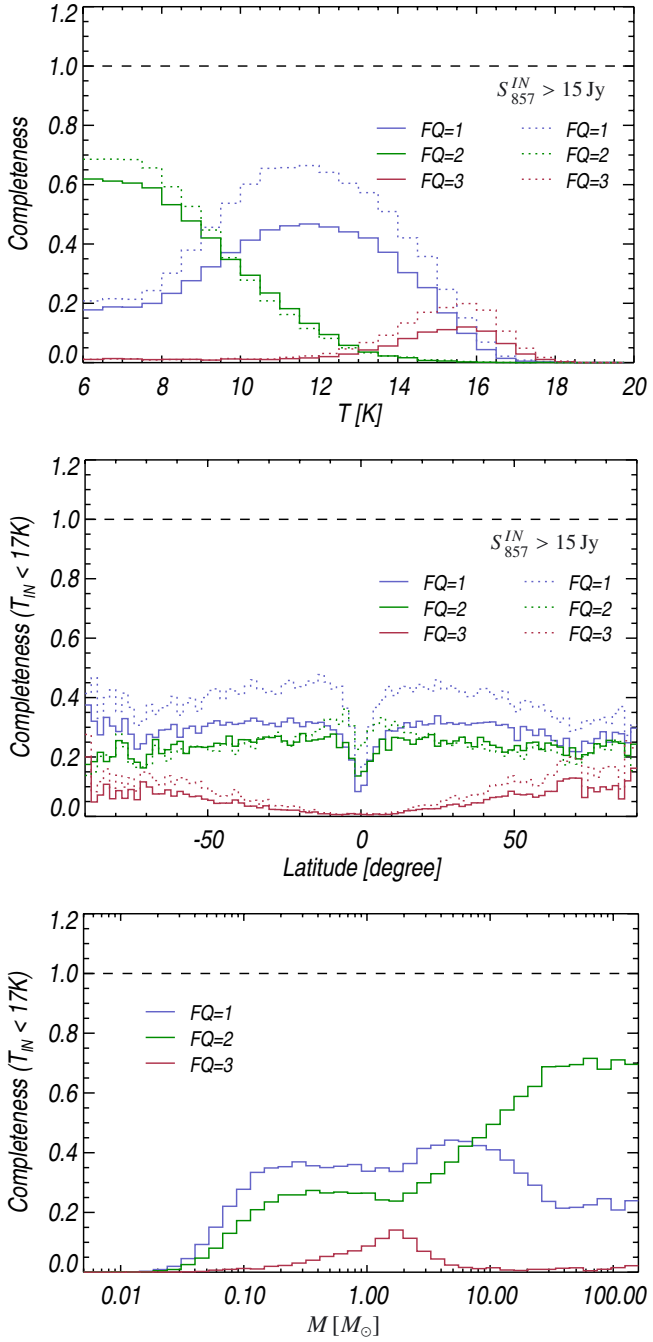

Fig. 4. Completeness as a function of the input temperature (*top panel*), latitude (*middle panel*), and mass (*bottom panel*) of the injected sources. For the latitude and mass cases, the input temperature was lower than 17 K. In addition, when considering the dependence of completeness on mass, all the sources are assumed to be at 100 pc from the Sun. Each panel shows the distributions obtained from selecting only the sources in a given FLUX_QUALITY category. In particular, FQ = 1, 2 and 3 correspond to the blue, green and pink curves, respectively. Finally, the dotted line in each panel denotes the completeness for the sample of sources with input flux density $S_{857} > 15$ Jy.

has an accuracy of 50% or more (dashed line), we obtain a result in agreement to within 1σ with the IRIS sensitivity limit, i.e., it drops to 0% for flux densities below 0.5 Jy. Interestingly, the completeness drops to 0% for S_{545} and S_{353} below 1 Jy and 0.3 Jy, respectively, for all FQ categories: these two bands define the detection limit of our catalogue.

This flux density limit can be converted into a mass detection limit if we assume that all the sources are located at 100 pc from the Sun. The completeness as a function of mass is shown in the bottom panel of Fig. 4. The catalogue appears very incomplete for sources with a mass below 0.1 $M_\odot$, which explains the lower cutoff of the PGCC mass distribution in Fig. 12. At the same time, for sources with FQ = 1 the catalogue is complete at the 20−40% level across the entire mass range, meaning that no mass selection is introduced by CoCoCoDeT. Therefore, the only (significant) bias introduced in the PGCC mass distribution originates from the availability of distance estimates. Finally, the simulated FQ = 2 detections are characterized by a higher degree of completeness for relatively high mass values, as also observed also for the PGCC sources.

4.3. Geometric accuracy

By *geometry*, we mean the ensemble of parameters (e.g., centroid, ellipticity, position angle and equivalent full width half maximum) that describes the location, size and orientation of the source. The accuracy of these parameters is crucial for accurate photometric measurements, as described in Sect. 2.3.

Figure 6 summarizes the catalogue positional accuracy, which we define as the offset between the input and the recovered centroid of the synthetic sources. The cumulative distributions are shown at four confidence levels: 68%, 90%, 95% and 99%. 68% of the sources have a recovered centroid with a 0.′2 uncertainty, and 95% with a 0.′8 uncertainty. The median of the position offset distribution is 10″. Thus, despite background confusion, our catalogue appears to contain accurate source coordinates.

We have also checked the accuracy for the other geometric parameters. For this purpose, we have investigated the relation between the ratio of the recovered to injected quantity (OUT/IN) and the S/N. The result is illustrated in Fig. 7.

For each bin in S/N, we have computed the cumulative OUT/IN distributions and corresponding median (solid line): in Fig. 7, each panel shows 68% (light shaded contours) and 95% (dark shaded contours) of the sources at a given frequency. The uncertainty on the recovered position angle (Fig. 7, middle panel) and ellipticity (Fig. 7, bottom panel) is very good, and below 10% for 68% of the sources at $S/N > 6$. When we include 95% of the sources at $S/N > 6$, the uncertainty varies between 20 and 30%. We note that for $S/N > 10$, the uncertainty on the recovered parameters remains fairly constant up to very high S/N. The reconstructed size of the sources, θ, (Fig. 7, top panel) appears more uncertain at all S/N, with an uncertainty of about ±15 to 20% for 68% of the dataat $S/N > 6$, and ±30% of uncertainty when we include 95% of the data. More importantly the recovered θ is systematically underestimated by about 10% compared to the injected one, due to background. This effect has a direct impact on the photometric accuracy, as discussed in the following section.

4.4. Photometric accuracy

Following a procedure similar to the one applied in the case of the geometric parameters, we have estimated the accuracy of the photometric measurements. Accordingly, we have computed the ratio of the recovered (OUT) to injected (IN) flux densities and analysed its behaviour as a function of S/N. We have limited the analysis to sources with FQ = 1 at 3 THz and FQ = 1 and 2 in the *Planck* bands.

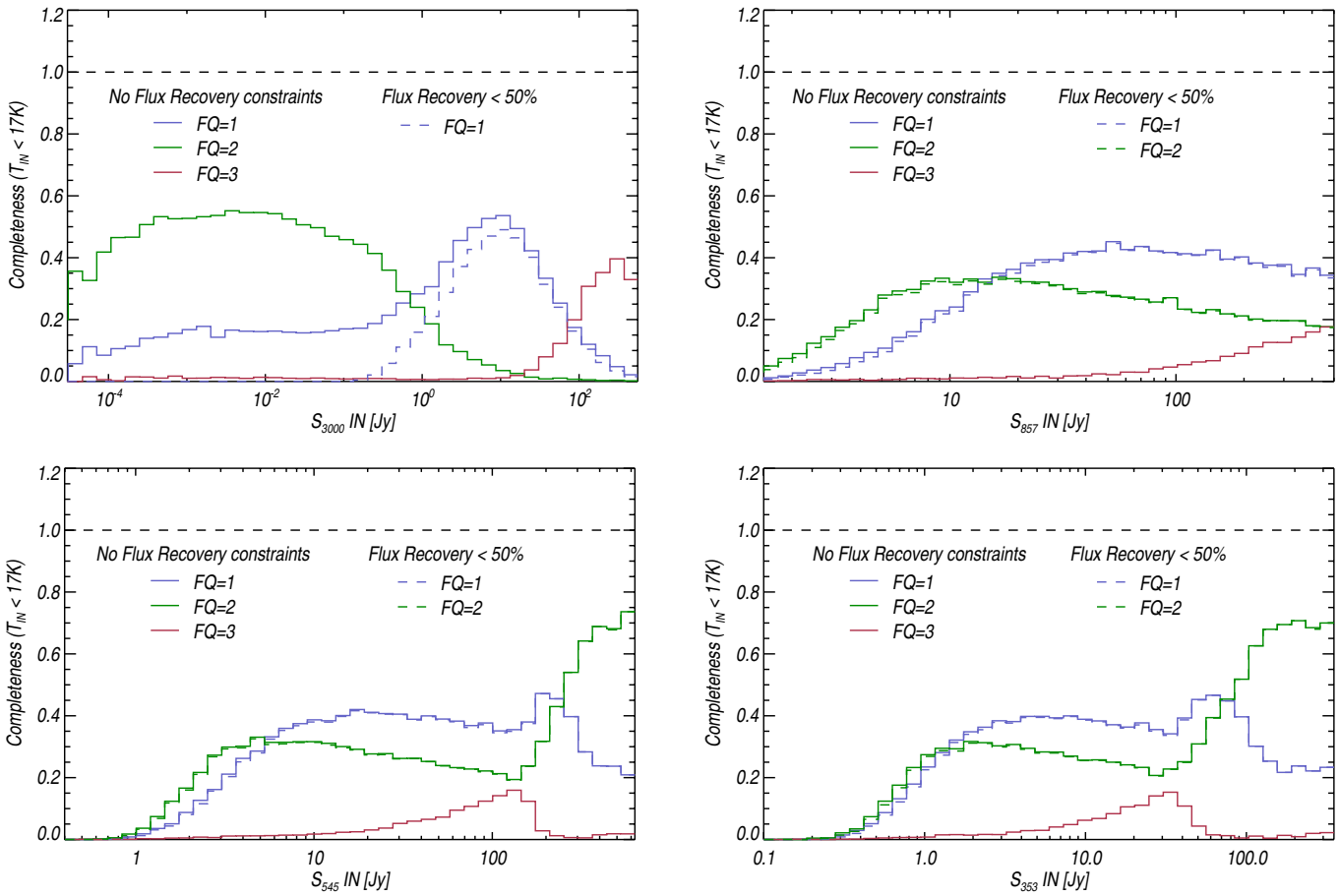

Fig. 5. Completeness (computed on a restricted sample of sources with injected temperature below 17 K) as a function of the injected flux density in the IRAS 3 THz (*top left panel*) and *Planck* upper frequency bands, 857 GHz (*top right panel*), 545 GHz (*bottom left panel*), and 353 GHz (*bottom right panel*). It is shown per-category of flux density quality, i.e., FQ = 1, 2 and 3 categories (blue, green and pink, respectively). The completeness is also computed on a more restricted sample of sources with injected temperature below 17 K and with a flux density accuracy better than 50% (dashed lines).

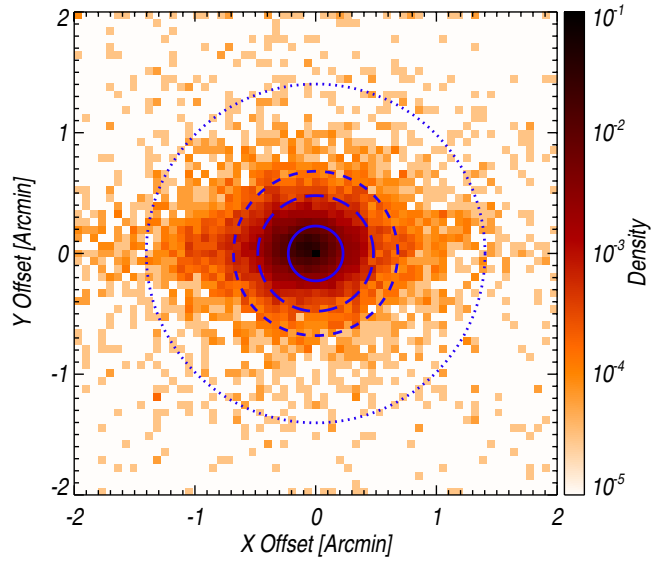

Fig. 6. Density distribution of the positional offsets computed from 100 000 Monte Carlo realizations. Circles show the cumulative distributions at 68% (solid line), 90% (long-dashed line), 95% (dashed line) and 99% (dotted line).

The poorest performance appears to be in the 3 THz band. The S/N has to be as large as 15 for the accuracy to reach a level of about 50% for 68% of the data, while the uncertainty is higher by a factor of 4 if we include 95% of the distribution. At lower S/N (<15), the OUT/IN ratio can reach a factor of 10, while, by definition of FQ = 1, it should be below 2 because of the $S^{\rm OUT}_{3000}/\sigma_{S^{\rm OUT}_{3000}} > 1$ contraint. Thus, the uncertainty at 3 THz is severely underestimated during the photometry measurement.

If we compute the ratio of the difference between the recovered and injected flux density to flux density uncertainty, $(S^{\rm OUT}_{3000} - S^{\rm IN}_{3000})/\sigma_{S^{\rm OUT}_{3000}}$, we find a mean value of 5. We interpret this result as due to the fact that, at this frequency, the performance of the photometric measurements is dominated by modelling uncertainties, such as the removal of the warm background. However, this effect does not introduce any bias on the flux density measurements at 3 THz.

The photometric accuracy of the photometry in the *Planck* bands (second, third and fourth panel from the top in Fig. 8) is much better than at 3 THz. Indeed the uncertainty goes down to less than 10% for 68% of the sources at $S/N > 6$, once the data are bias-corrected. In fact, the flux densities in the *Planck* bands are systematically underestimated, i.e., by 10% at low S/N and by 5% at high S/N, as a consequence of the underestimation of θ (see Sect. 4.3), a well-known effect also studied in the framework of both the ERCSC Planck Collaboration VII (2011) and the PCCS Planck Collaboration XXVIII (2014), Planck Collaboration I (2016). This bias is about at the same

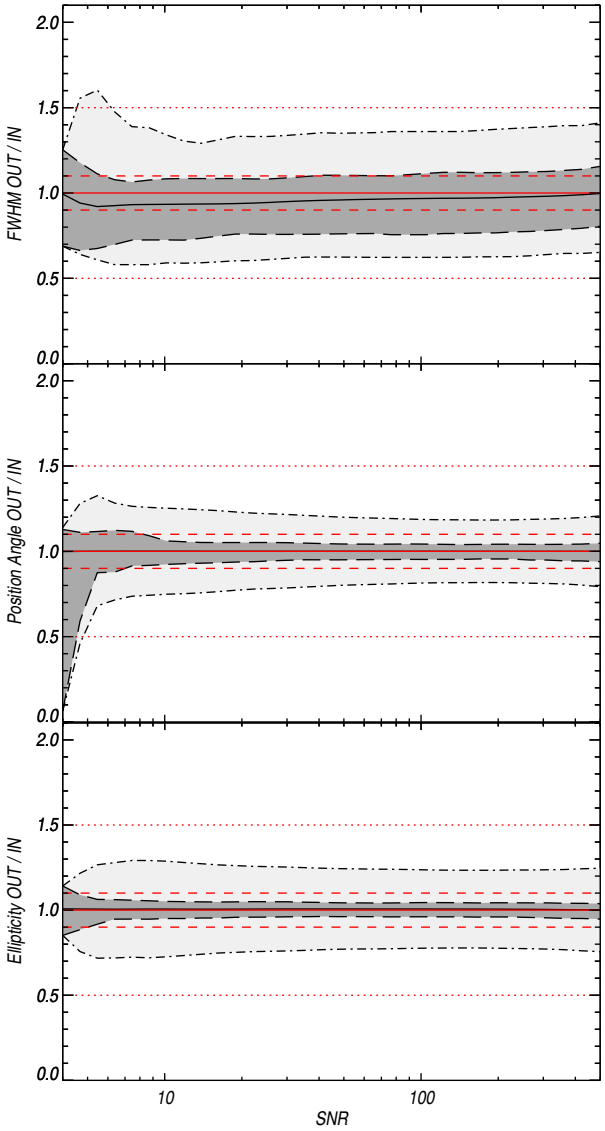

Fig. 7. Ratio of the recovered (OUT) to injected (IN) geometric parameters for the simulated sources detected with FQ = 1 and 2: θ (*top*), position angle (*middle*) and ellipticity (*bottom*). The ratio is given as a function of the detection S/N estimated from the cold residual maps. The light and dark grey shaded regions (denoted by the dot-dashed and long-dashed lines, respectively) highlight the behaviour of 95% and 68% of the sources, respectively, in each S/N bin. The median of the ratio distributions are shown with a solid line. The 0%, 10% and 50% levels of uncertainty are overlaid using a red solid, dashed and dotted line, respectively.

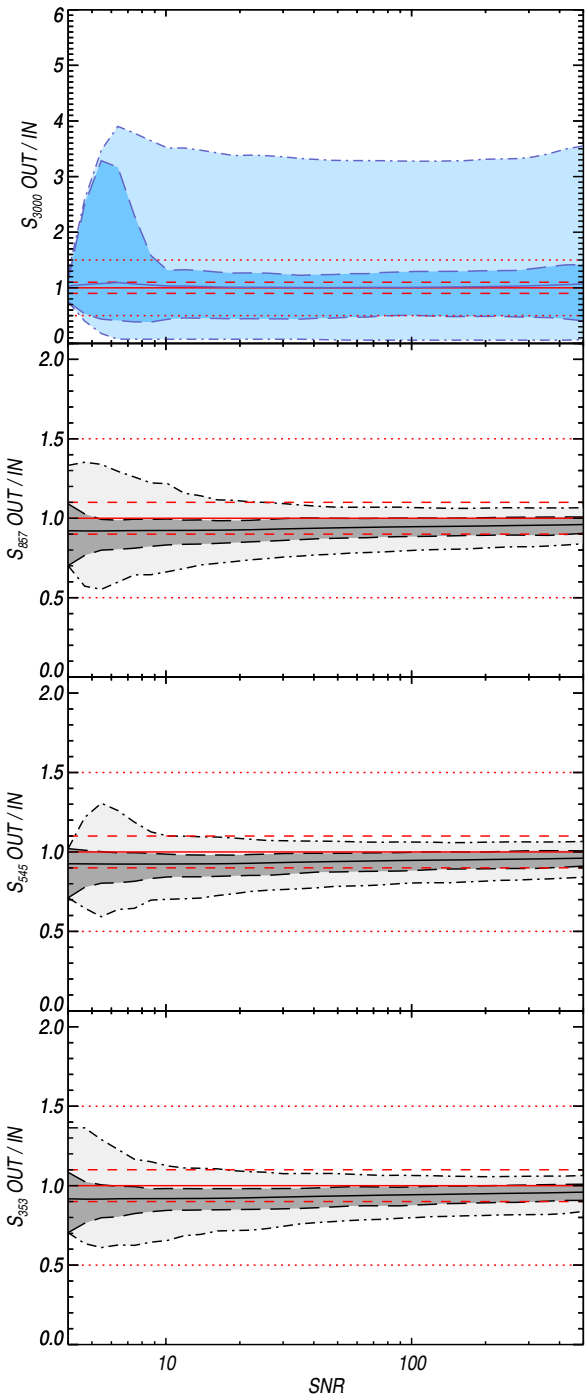

Fig. 8. Ratio of the recovered (OUT) to injected (IN) flux densities for the simulated sources detected with FQ = 1 and 2. The ratio is given as a function of the detection S/N estimated from the cold residual maps. The light and dark grey shaded regions (denoted by the dot-dashed and long-dashed lines, respectively) highlight the behaviour of 95% and 68% of the sources, respectively, in each S/N bin. We note that at 3 THz (*top panel*) we only consider sources with FQ = 1, and the corresponding contours and shaded regions are highlighted in colour. The median of the ratio distributions are shown with a solid line. The 0%, 10% and 50% uncertainty levels are overlaid using a red solid, dashed and dotted line, respectively.

level as the flux density uncertainty, thus it is included in the 1σ uncertainty.

5. Distance estimates

In this section we describe the derivation of the distance estimates for the PGCC sources which have been obtained by using four different methods: i) cross-checking with kinematic distance estimates already available; ii) using the optical or near-infrared extinction due to the PGCC sources as an indicator of their distance; iii) associations with known molecular complexes; iv) estimates from the literature.

5.1. Kinematic

The Simon et al. (2006a) and Jackson et al. (2008) catalogues of infrared dark clouds (IRDC) provide kinematic distances

for 497 objects. These distances are obtained by combining the gas observed radial velocity with a Galactic rotation curve, in the assumption of gas circular motion. Accordingly, an observed radial velocity at a given longitude corresponds to a unique Galactocentric distance solution while, at least in the inner Galaxy, two heliocentric distances are allowed. By cross-correlating the PGCC sources with the IRDC catalogues in a 5′ radius, we have found 92 associations, mainly located along the Galactic plane. To these sources we have assigned the distance flag `DIST_KINEMATIC`. We note that, when two heliocentric solutions are available, we always choose the near solution. An arbitrary 25% uncertainty on these distance estimates is adopted. In the following, we will refer to kinematic distances as method [1].

5.2. Optical extinction

Distances derived from optical extinction are based on processing of two independent Sloan Digital Sky Survey (SDSS) photometry-based data sets containing the computed distances and interstellar reddening to each star. The first data set, based on SDSS DR7 photometry and covering 1467 PGCC sources, is that of Berry et al. (2012) who fit reddening and the stellar locus colours of Covey et al. (2007) to the observed photometry. The second data set, from Mc Gehee (in prep.), makes use of the SDSS DR9 catalogue. This targets a total of 1769 cold clumps and computes the reddening from $g-i$ colour excess, where the intrinsic stellar $g-i$ colour is derived from the reddening invariant indices defined by McGehee et al. (2005).

Distance moduli values and uncertainties for each cold clump are inferred from analysis of 100 Monte Carlo runs using stars within a 10′ radius of the catalogue position. For each realization the distance moduli and $E(B-V)$ reddening of each star are randomly varied assuming normal distributions of $N(0, 0.282^2)$ and $N(0, 0.072^2)$, respectively, These variance values, which are similar for both data sets, were computed by propagating the observed stellar locus width in low extinction ($A_r < 0.05$) regions and the stated photometric uncertainties through the relations for $E(B-V)$ and $m-M$.

Each of these profiles are processed by a Canny edge detection filter (Canny 1986) with the location of the cold clump set by the distance modulus for which the edge detection signal is maximized. A Gaussian sigma of 0.3 mag in $m-M$ is used in the Canny filter for smoothing and noise reduction. Implicit in this approach is the assumption that there is only a single interstellar cloud along the line-of-sight. For each PGCC source we assign a value and uncertainty to the distance modulus based on the mode and standard deviation of the distribution. This distribution is obtained via kernel density estimation [KDE] on a 0.01 mag grid using the values returned from the Monte Carlo realizations and with the bandwidth of the KDE set by the normal distribution approximation.

We adopted the following prescriptions of Mc Gehee (in prep.) to build a final selection of robust distance estimates: i) distance estimates obtained with the M dwarf based technique (Mc Gehee, in prep.) towards sources with an extinction $E(B-V) < 0.4$ are rejected; and ii) distance modulus estimates with uncertainties larger than 1.0130 and 0.7317, for the Berry et al. (2012) or Mc Gehee (in prep.) methods, respectively, are also rejected. Furthermore we have performed a sanity check on the altitude of the sources, rejecting those with an altitude above or below 2 times the Galactic scale height, which has been recently estimated by Jones et al. (2011) at 119 ± 15 pc.

Two sets of distance estimates are finally provided using optical extinction with SDSS data, depending on the SDSS data version. Hence 1083 sources have been assigned a distance estimate based on the DR7 SDSS data version using the Berry et al. (2012) method [2] (distance flag `DIST_OPT_EXT_SDSS_DR7`) and 191 sources based on the DR9 SDSS data version using the Mc Gehee (in prep.) method [3] (distance flag `DIST_OPT_EXT_SDSS_DR9`).

5.3. Near-infrared extinction

By comparing observed stellar colours to the predictions of the Besançon Galactic model (Robin 2003, 2012), we have attempted to infer the most probable three-dimensional extinction distribution along the line-of-sight. The line-of-sight extinction is parametrized using a number of points, each described by a distance and an extinction. These parameters are probed using a Markov chain Monte Carlo (MCMC) method, based on the Metropolis Hastings algorithm with 10^5 iterations. Modelled stars are reddened using linear interpolation between points and comparison with observations is performed on the colour distribution using a Kolmogorov Smirnov test.

Stars are chosen from the Two Micron All Sky Survey (2MASS, Skrutskie et al. 2006) point source catalogue that lie within the ellipse defining the cold clump, so in the location of the cloud along the line-of-sight should be detectable as a sharp rise in extinction. The resultant extinction vs. distance profile is then analysed to detect the presence of any clouds. The dust density with respect to distance is calculated via the derivative of the extinction distance relation and the diffuse extinction is estimated from the continuum. Any peaks in dust density 3σ over the diffuse are flagged. If a line-of-sight contains more than one cloud, the one with the highest extinction is chosen and the presence of a second cloud is flagged. Only lines-of-sight with a single detected cloud have been included in the present PGCC catalogue.

The principle of the method is similar to that described by Marshall et al. (2006) and Marshall et al. (2009). The motivation for the change in our case is to provide more robust estimates when stellar density is low, as well as to more fully characterize the uncertainty via the MCMC exploration of the parameter space.

The former version of this method was first applied in Marshall et al. (2009) on the Simon et al. (2006a) *MSX* catalogue of IRDCs, providing 1218 distance estimates. After cross-correlating the PGCC sources with this IRDC catalogue using a 5′ radius, we have found 182 associations, leading to the distance estimates of the method [4] (`DIST_NIR_EXT_IRDC` field). We have adopted an uncertainty for the distance estimate of 25% following Marshall et al. (2009) prescriptions. The improved algorithm has been then applied to the PGCC sources using 2MASS data. After performing the sanity check on the altitude (as for the optical extinction methods), and including 787 upper limits (marked as negative estimates), this has led to 2810 estimates (method [5], `DIST_NIR_EXT` field). The uncertainty on these new set of distance estimates is provided individually by the algorithm.

5.4. Molecular complexes

A simple inspection of the all-sky distribution of cold clumps (see Fig. 1) suggests that it follows the distribution of known molecular complexes at intermediate latitude, as it is illustrated

Table 3. Molecular complexes used to assign a distance estimate to the PGCC sources. For more details see Sect. 5.4.

Name	l [deg]	b [deg]	Area [deg^2]	Distance [pc]	No.
Aquila Serpens .	28	3	30	260 ± 55[1,2]	51
Polaris Flare . . .	123	24	134	380 ± 40[3]	68
Camelopardalis .	148	20	159	200 ± 30[3]	19
Ursa Major	148	35	44	350 ± 35[3]	22
Taurus	177	−15	440	140 ± 15[2]	384
Taurus Perseus . .	163	−15	440	230 ± 20[2]	224
λ Ori	196	−13	113	400 ± 40[4]	70
Orion	212	−9	443	450 ± 50[2]	333
Chamaeleon	300	−16	27	170 ± 15[5]	114
Ophiuchus	355	17	422	150 ± 5[2]	316
Hercules	45	9	35	300 ± 75[6]	19

Notes. [(1)] Bontemps et al. (2010); [(2)] Loinard (2013); [(3)] Schlafly et al. (2014); [(4)] Murdin & Penston (1977); [(5)] Bertout et al. (1999); [(6)] Andersson et al. (1991).

Table 4. Number of sources with a distance estimate for each of the seven methods, before (Col. 2) and after (Col. 3) the combination process described in Sect. 5.6, in which only one distance is selected among the ones available.

Method	No		DIST_QUALITY			
	Init.	Final	1	2	3	4
[1] Kinematic . . .	92	23	–	23	–	–
[2] Opt. Ext. DR7	1083	719	–	717	2	–
[3] Opt. Ext. DR9	191	173	63	89	21	–
[4] NIR Ext. IRDC	182	106	19	81	6	–
[5] NIR Ext.	2810	2491	138	1601	88	664
[6] Complexes . .	1895	1834	177	1576	81	–
[7] HKP-GCC . . .	228	228	67	104	57	–
Total		5574	464	4191	255	664

Notes. The repartition between methods of the final distance estimates provided in the catalogue (DIST field) is shown in Cols. 4 to 7 for each category of the distance quality (DIST_QUALITY flag): Consitent (1), Single (2), Unconsistent (3), Upper limit (4).

in Appendix B. Many of these molecular complexes have distance estimates in the literature. To assign the distance of a complex to a particular cold clump, we have used the all-sky CO *Planck* map. In particular, we have checked the presence of a given PGCC source inside a molecular cloud, by using a mask generated from the CO map. This method has been applied to 11 molecular complexes listed in Table 3 and located outside the Galactic plane, which allows us to minimize the effect of confusion. Following this procedure, we have obtained 1895 distance estimates (method [6], DIST_MOLECULAR_COMPLEX field) with associated uncertainties.

5.5. Herschel follow-up

As mentioned in the introduction and further discussed in Sect. 7 we have performed a high angular resolution follow-up with the PACS and SPIRE instruments on-board *Herschel*, in the framework of the *Herschel* key-programme Galactic Cold Cores (HKP-GCC). This follow-up programme has targeted 349 PGCC sources, for which we have obtained distance estimates from the literature (Montillaud et al. 2015), the most reliable of which (228 sources) are reported in the final catalogued and flagged as DIST_HKP_GCC field. In the following, we refer to this method as method [7].

5.6. Combined distance estimates

We rank all methods by increasing order of confidence level, starting with the kinematic estimates ([1]), which several authors indicate as less reliable than extinction estimates (Foster et al. 2012), due to the distance ambiguity in the inner Galaxy. The estimates derived from optical extinction are ordered as [2] then [3], according to the SDSS data release version (DR7 to DR9). The estimates obtained from the near-infrared extinction come next, starting from those obtained towards IRDCs ([4]), and then considering the ones from the improved algorithm ([5]). The association with molecular complexes ([6]) provides consistent estimates for sources belonging to the same cloud. Finally, the distance estimates derived from the analysis of the *Herschel* observations appear as the most reliable ([6]).

In the final catalogue we have assigned to each source a unique distance value (DIST), corresponding to the distance estimate with the highest confidence level among the available estimates. This approach allows us to avoid assigning to a source an average distance computed from individual estimates obtained from very different methods. Importantly, we have checked the internal consistency among the available estimates for a given clump using the following relation,

$$X_{\rm D} = \sqrt{\frac{1}{C_n^2}\sum_{i\neq j}\left(\frac{|D_i - D_j|}{\sigma_i + \sigma_j}\right)^2} < 1, \quad (1)$$

where n is the number of available distances, D_i and D_j are the distance estimates and their corresponding standard deviation σ_i and σ_j, and C_n^2 is the number of combinations of pairs between the n estimates. A value $X_{\rm D} < 1$ indicates that the mean distance between distance estimates is compatible with a 1σ uncertainty on each estimate. We have used the $X_{\rm D}$ parameter to assign a DIST_QUALITY flag to each source. In particular, $X_{\rm D}$ can take up the following values:

0. "No estimate": no distance estimate available;
1. "Consistent": few estimates are available and consistent within 1σ ($X_{\rm D} \leq 1$);
2. "Single": one single estimate;
3. "Unconsistent": few estimates are available, but not consistent within 1σ ($X_{\rm D} > 1$);
4. "Upper limit": only an upper limit is available.

Following the procedure described above, we have obtained a total of 5574 distance estimates distributed across the whole sky with an associated DIST_QUALITY flag. The method selected for each distance estimate (DIST) is specified with the DIST_OPTION field, which ranges from 0 to 7 (see Table 4). The statistical properties of the distance distribution are shown in Table 4. We emphasize that these distance estimates have been compiled without taking into account the quality of the photometric measurements. In total, there are 4655 PGCC sources with DIST_QUALITY flag equal to 1 and 2. Of these, only 2489 sources have reliable flux densities in all bands (FQ = 1), while 1378 sources have reliable flux densities in the *Planck* bands, but not at 3 THz (FQ = 2). For more details see Table 5.

The cross-correlation between the DIST_QUALITY and FLUX_QUALITY flags is shown in Table 5, and reveals that

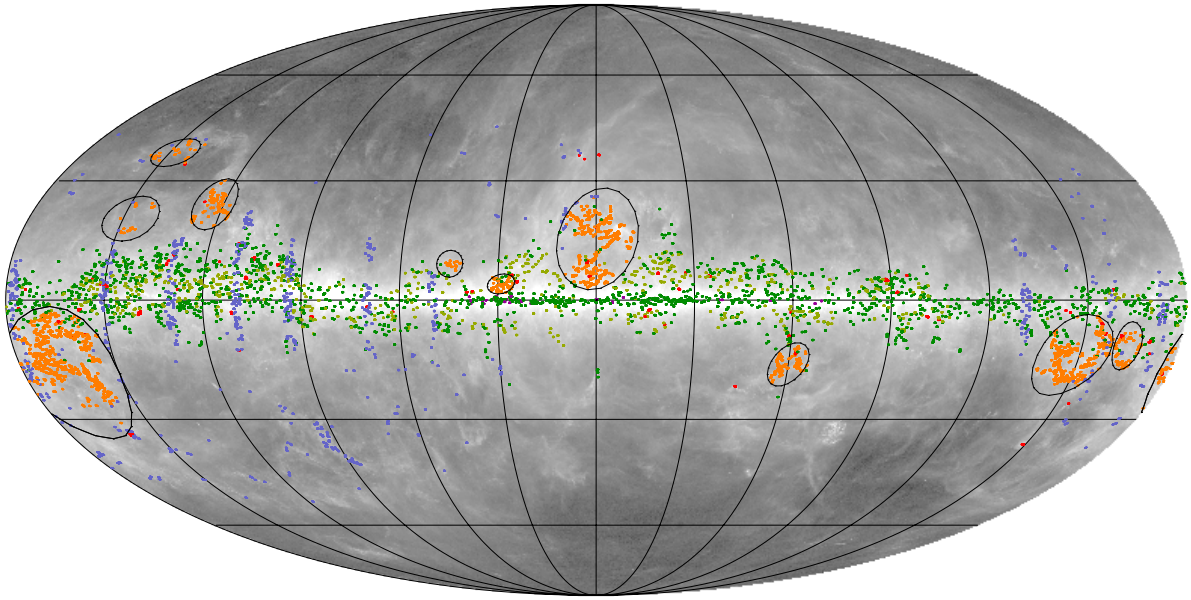

Fig. 9. All-sky distribution of the 4655 PGCC sources for which a distance estimate with a DIST_QUALITY flag equal to 1 or 2 is available. The various types of distance estimates are defined as follows: kinematic (purple), optical extinction (blue), near-infrared extinction (green), molecular complex association (orange), and *Herschel* HKP-GCC (red). We also show the distribution of the 664 sources with an upper-limit estimate (DIST_QUALITY=4) provided by the near-infrared extinction method in light green. The regions covered by the molecular complexes are shown as black contours (see Table 3).

Table 5. Number of sources with a distance estimate in each category of the DIST_QUALITY and FLUX_QUALITY flags.

DIST_QUALITY	FLUX_QUALITY		
	1	2	3
1	240	146	78
2	2249	1232	710
3	116	88	51
4	335	220	109

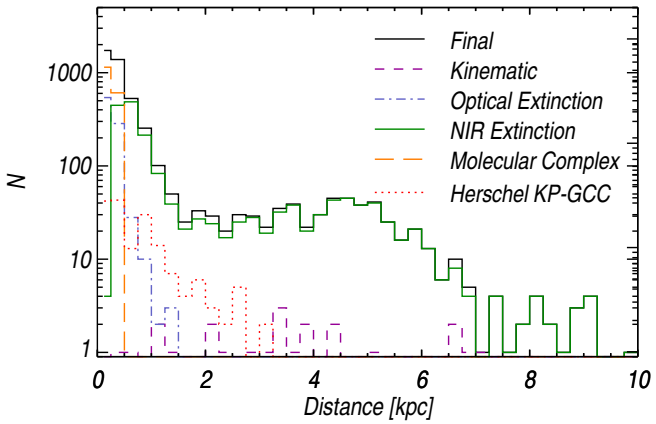

Fig. 10. Distance distribution per type: kinematic, optical extinction, near-infrared extinction, molecular complex association, and *Herschel* HKP-GCC.

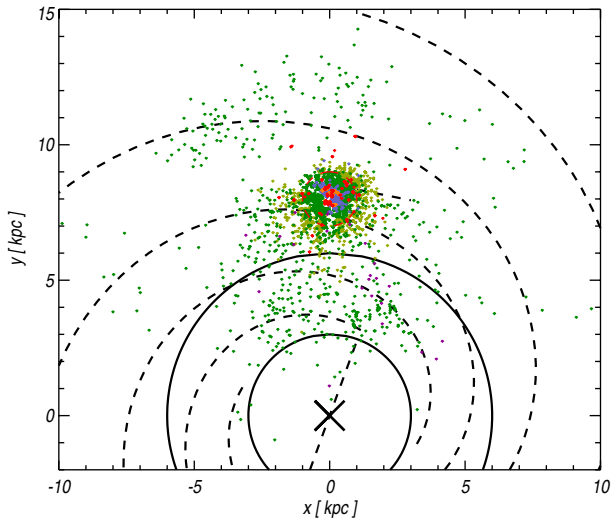

Fig. 11. Distribution of the PGCC sources as seen from the north Galactic pole. Only distance estimates with a DIST_QUALITY flag equal to 1 and 2 are plotted. Different methods have been used to derive the distances: kinematic (purple), optical extinction (blue), near-infrared extinction (green), molecular complex association (orange), and *Herschel* HKP-GCC (red). We also show the distribution of the distance upper-limits (DIST_QUALITY=4) provided by the near-infrared extinction method (light green). The red dashed circle shows the 1 kpc radius around the Sun. Black dashed lines represent the spiral arms and the local inter-arm spur in our Galaxy. The black circles, centred on the cross, provide an indication of the location of the molecular ring.

only 2489 sources have both reliable distance estimates DIST_QUALITY=1 or 2) and reliable flux densities in all bands (FQ = 1), while 1378 sources have reliable flux densities in *Planck* bands but not at 3 THz (FQ = 2).

The spatial distribution of the sources having a distance estimate (see Fig. 9) strongly depends on the adopted distance method. Hence, sources with distances derived from optical extinction (blue) mainly follow the SDSS sky-coverage, which presents large stripes over the sky. Distances obtained from associations with molecular cloud complexes present a patchy distribution, mirroring that of the host clouds (orange). The near-infrared extinction estimates (green) are mostly concentrated towards the inner Galactic plane where the density of stars

is sufficient to provide high extinction contrast, while the near-infrared extinction upper-limit estimates (light green) are spread at larger latitudes for the same reason.

A similar type of consideration applies to the analysis of the statistical distribution of all distance estimates (see Fig. 10). The near-infrared extinction and kinematic methods allows us to probe distant regions (from 1 kpc to 9 kpc) across the Galactic plane. On the contrary, the optical extinction and molecular complex associations methods are only applicable in the nearby Galaxy (up to 1 kpc and 0.5 kpc, respectively). As seen from the north Galactic pole (Fig. 11), the complementarity of the different methods shows clearly. About 88% of the sources with a reliable distance estimate (DIST_QUALITY=1 or 2) lie within 2 kpc from the sun. Therefore, the PGCC catalogue mainly probes the solar vicinity. It is interesting to notice that the distribution of the PGCC sources at larger distance follows at first order the Galactic arms and the molecular ring. This is especially significant for the Perseus arm towards the outer Galaxy and for the Scutum-Centaurus and Norma arms in the inner Galaxy. We conclude this section by emphasizing that, due to the variety of distance estimators, any statistical analysis involving distances or the related quantities, will be affected by severe biases which, given that the catalogue is not flux density complete, are very hard to quantify.

6. Physical parameters

For the *Planck* Galactic cold clumps we have derived: temperature, column density and, when distance estimates are available, size, mass, mean density and luminosity. The propagated uncertainties on the computed quantities are obtained, for each clump, from 10^6 Monte Carlo simulations and are provided in two different fashions: i) as 1σ standard dispersion; ii) as defined by the lower and upper limits of the 68%, 95% and 99% confidence intervals of the Monte Carlo distributions. The latter takes into account the non-Gaussian behaviour of the same Monte Carlo distributions.

Figure 12 illustrates the temperature, column density, size, mass, mean density and luminosity distributions for the PGCC sources with FLUX_QUALITY equal to 1 and 2. We note that sources with FQ = 1 have reliable flux densities in both the IRIS 3 THz and *Planck* bands, which allows the derivation of reliable temperatures and emissivity index, while sources with FQ = 2 are likely faint and cold, and their temperatures estimated are obtained using only the three *Planck* bands and a fixed emissivity spectral index of 2. In the case of physical quantities for which a distance estimate is needed, we also require that DIST_QUALITY is either 1 or 2.

Additionally, we investigated the impact of the individual uncertainties estimated above on the overall source catalogue distribution for each physical quantity. To this end, we have again used a Monte Carlo approach. In this case, for each quantity, we build 10 000 synthetic samples with the same number of sources as the original sample. Then, starting from the computed values, we add random noise based on the uncertainty associated with each source. At this stage, we generate the 1σ upper and lower contours for each of the 10 000 samples, where the 1σ limit is estimated based on the median of the distribution. Figure 12 shows, as expected, that the contours follow reasonably well the distribution of the computed values when the uncertainties are relatively small. On the contrary, there is quite a significant departure from these when the uncertainties are large.

6.1. Temperature and emissivity

The source temperatures and the local warm background temperatures have been estimated using the flux density measurements and their corresponding uncertainties in the IRIS 3 THz band and the *Planck* 857, 545, and 353 GHz channels (see Sect. 2.3). The fits of the SEDs have been performed assuming that the emission can be described as a modified black body,

$$F_\nu = F_{\nu,0} B_\nu(T)(\nu/\nu_0)^\beta, \quad (2)$$

where F_ν are the observed flux densities, β is the emissivity spectral index, T is the fitted colour temperature, and $F_{\nu,0}$ is the fitted flux density at a reference wavelength ν_0. In Eq. (2) we have assumed that the observed emission is optically thin at frequencies $\nu \leq 3$ THz, that the emissivity spectral index is constant within the fitted wavelength range, and that the source is isothermal. The first two assumptions likely hold, however, the sources are not necessarily isothermal. In particular, the temperature is expected to vary along the line-of-sight due to radiative transfer effects, with lower values in the inner, denser part of the clump than the averaged colour temperature obtained from Eq. (2). The derived column density and mass can then be underestimated up to a factor of 3 (Ysard et al. 2012). For each source, two independent temperature estimates have been obtained, i.e., by fixing the emissivity spectral index, β, to 2.0, or by letting β be a free parameter. These estimates and their uncertainties have been calculated with a MCMC approach, using a Bayesian formulation with flat priors distributions for the temperature, emissivity spectral index (when this is a free parameter), and the amplitude of the fitted modified black body (see Juvela et al. 2013, and references therein). The allowed parameter ranges are: $5.0 < T < 30$ K, $0.5 < \beta < 5.0$ and $F_{\nu,0} > 0.0$.

The MCMC calculations have been made in chunks of 10^7 iterations. After reaching convergence (following the initial burn-in phase), the parameters have been estimated from the final 5×10^7 steps. The parameters values quoted in the catalogue correspond to the mean and the marginalized 68% confidence intervals calculated from the MCMC samples. The uncertainty of the MCMC temperature estimate caused by the finite length of the MCMC chain is always negligible.

For sources with FQ = 1, we have compared the temperature and emissivity spectral index obtained from χ^2 fits and from the MCMC results, and these are on average within 1%. For sources with the lowest S/N, the χ^2 method tends to give higher T values and lower β values than the MCMC technique. This is consistent with the behaviour found in simulations where, when β is treated as a free parameter, the joint probability distribution of T and β is asymmetric and presents a long tail towards low temperatures and high values of the emissivity spectral index (Juvela & Ysard 2012; Shetty et al. 2009). The standard deviations of the MCMC vs. χ^2 estimates are $\sigma(T) = 0.3$ K and $\sigma(\beta) = 0.08$. Again, these numbers reflect mostly the behaviour of sources with the lowest S/N measurements. In general, the difference between the MCMC and χ^2 estimates are not significant when compared to the uncertainties. The MCMC results have also been compared to χ^2 fits performed over a regular grid with a step $\Delta T = 0.2$ K and $\Delta\beta = 0.05$, where, at each grid position, we fit only the amplitude of the model spectrum. The results are consistent within the uncertainties, confirming that MCMC has correctly localized the absolute minimum across the entire allowed parameter space.

We stress that the temperature estimates of the sources correspond to the temperature of the clump-only after removal of the

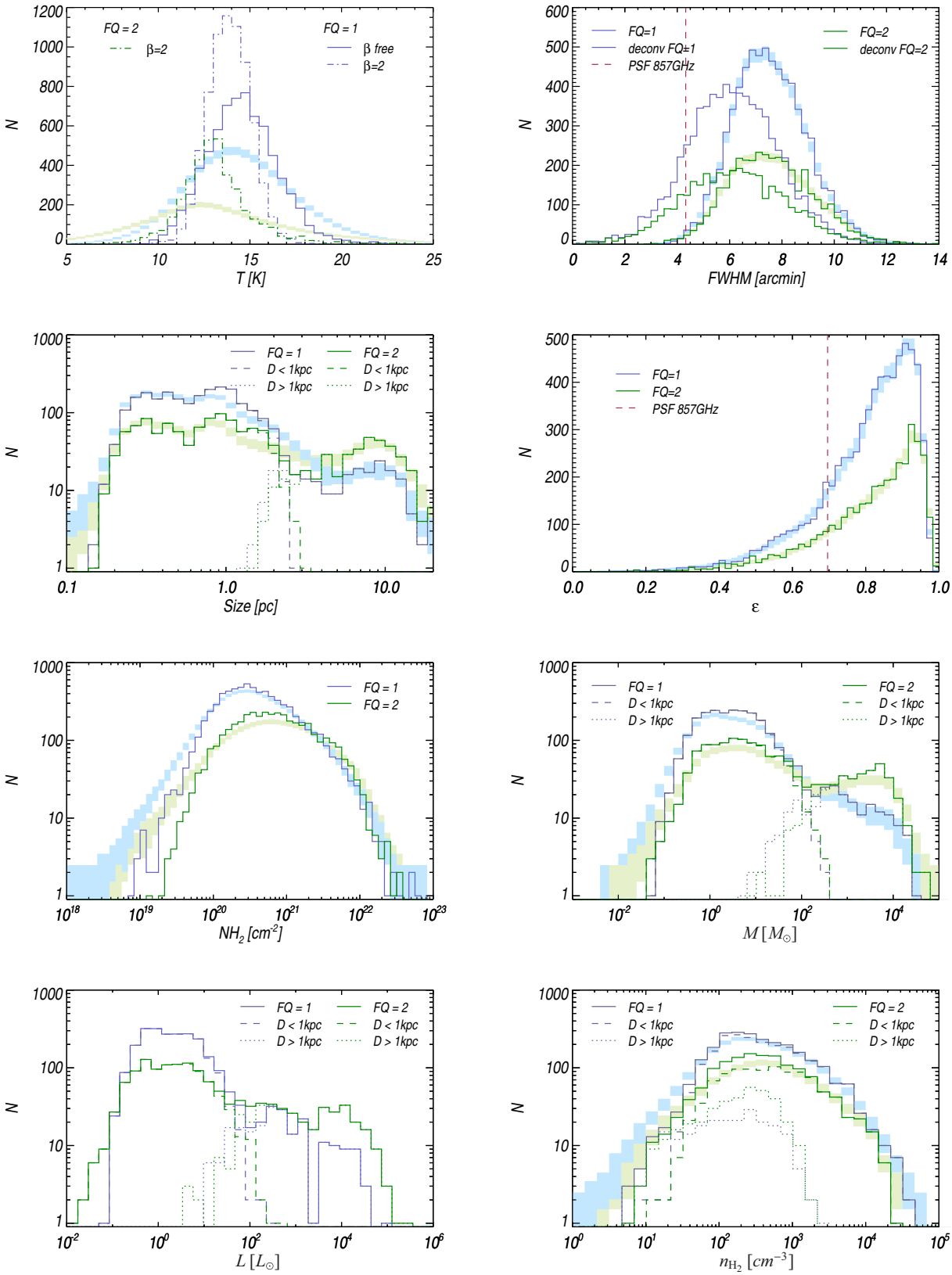

Fig. 12. Distribution of the physical properties of the PGCC objects with FQ = 1 (blue) and FQ = 2 (green). The coloured shaded regions provide an estimate of the impact of the individual uncertainties on the statistical distribution at a 1σ dispersion level around the mean value obtained from 10 000 MC realizations (see Sect. 6 for more details). The temperature distribution is shown for two temperature estimates, i.e., using a free emissivity spectral index β (solid line) or a fixed $\beta = 2$ (dot-dashed line). The distribution of the intrinsic size, after deconvolution, is shown on the *top right panel* in dot-dot-dot-dashed line. The distributions of the physical size, mass, mean density and luminosity of the clumps are provided for sources with reliable distance estimates (`DIST_QUALITY`=1 or 2). These distributions are also shown separately for sources at solar distances smaller or larger than 1 kpc from the Sun, in dashed and dotted lines, respectively.

warm background, while the colour temperature is usually associated with the total emission on the line-of-sight. The resulting clump temperature distribution is shown in Fig. 12 for the two categories of sources, with FQ = 1 and 2. When the emissivity spectral index β is allowed to vary (solid lines), the temperature of the *Planck* cold clump candidates with FQ = 1 ranges from 8.6 to 30 K, and actually from 10.5 to 19.9 K when excluding the 2% extreme percentiles, with a peak of the distribution at about 14.5 K. Likewise, when we take $\beta = 2$, the distribution is narrower (ranging from 6 to 22.5 K, and from 11.1 to 16.8 K when excluding the 2% extreme percentiles) but still peaks around 14 K. These values are about 1 K higher than the temperature estimates derived in Planck Collaboration XXIII (2011). This can be ascribed to the change in calibration of the *Planck* high frequency bands (857 and 545 GHz) with respect to the data used for the *Planck* Early Papers and the *Planck* Results 2013 (see Planck Collaboration VIII 2014). The temperature distribution of sources with FQ = 2 has a peak at lower temperatures, around 13 K, and spans a range of lower temperatures, down to 5.8 K, while it ranges from 8.6 to 22.3 K when excluding the 2% extreme percentiles. This is consistent with the aforementioned hypothesis that these sources are colder than sources with FQ = 1.

If we compare this actual distribution with the expected temperature completeness of Fig. 4, we find that the temperature distribution of the PGCC sample with FQ = 1 drops to zero below 9 K, while the expected detection efficiency is still about 15% below 8 K for the same category. Considering now sources with FQ = 2, about 0.5% of the sample exhibits temperature below 8 K, but no sources below 5.8 K, where the expected completeness reaches almost 45% for the same category. The lower temperature limits at 8.6 and 5.8 K for sources with FQ = 1 and 2, respectively, appear therefore as physical thresholds, rather than a bias introduced by the detection algorithm. However, it is important to keep in mind that colder sources (below 6 K) may still exist on smaller angular scales.

6.2. Size

The geometric parameters of the PGCC sources are derived from the photometric measurements by means of an elliptical Gaussian fit to the 857 GHz cold residual map with an elliptical Gaussian. From the fit, we can estimate: the source centroid, its major and minor axis, ellipticity and position angle. In the catalogue, these quantities are available only for sources with FQ = 1 or 2.

The distribution of θ, defined as the geometric mean of the major and minor FWHM, $\theta = \sqrt{\theta_{\rm maj}\theta_{\rm min}}$, is shown in Fig. 12. The PGCC sources have an average θ of 7′.5 (red dashed line), thus appearing slightly extended with respect to the effective beam, $\theta_{\rm PSF}$, at 857 GHz (4.′325±0.′055, Planck Collaboration I 2014). We have also computed the intrinsic size, θ_i, of the sources by deconvolution of the observed diameter from the effective beam, and yielding an average value of 5.′6. We have obtained an average $\theta_i/\theta_{\rm PSF}$ ratio of 1.4, which is consistent with other similar observations, e.g., by BLAST (1.1, Netterfield et al. 2009) and Bolocam (1.5, Enoch et al. 2007). This effect might have to do with the hierarchical structure of the interstellar medium, and to the fact that cold clumps are likely to be characterized by the presence of extended envelopes. We note that, statistically speaking, PGCC sources with FQ = 1 or 2 have comparable θ distributions.

The ellipticity of the sources is defined as

$$\varepsilon = \sqrt{1 - \left(\frac{\theta_{\rm min}}{\theta_{\rm maj}}\right)^2}. \quad (3)$$

As shown in Fig. 12, PGCC clumps exhibit a distribution of the ellipticity peaking around 0.9 with a median value of 0.83, larger than the average ellipticity of the effective beam at 857 GHz, which is about 0.70 (Planck Collaboration I 2014). While the uncertainty on the major and minor FWHM determination can lead to an artificial elongation of the sources, we estimate that a 45% level of uncertainty is required to produce a median value of the ellipticity of 0.83 instead of 0.7, whereas the effective accuracy of the recovered ellipticity is about 10% (see Sect. 4.3). Therefore, the observed elongation of the PGCC sources cannot be explained by noise alone. Furthermore, we have verified that the position angle of the PGCC sources is not correlated with the *Planck* scanning strategy. Indeed, for the previous catalogue version, particularly the ECC (Planck Collaboration VII 2011), a statistical analysis revealed that the orientation of the sources was slightly spatially correlated with the scan direction. Such an effect was induced by the instrument transfer function, which at the time was not fully characterized. This issue has been resolved in the public release of *Planck* data (see Planck Collaboration VII 2014) used to build the present catalogue. About 40% of sources have $0.87 < \varepsilon < 0.95$, which translates to axial ratios between 2 and 3. PGCC clumps appear therefore clearly elongated, which may be due to their association with filamentary structures.

For the sources with a reliable distance estimate (`DIST_QUALITY`=1 or 2), i.e., 2489 and 1378 sources with FQ = 1 and 2, respectively, we have also derived their linear size. A few things need to be noted regarding the linear size distribution shown in Fig. 12. First of all, this distribution is limited to objects for which a distance estimate is available, and these constitute, as discussed in Sect. 5, a very heterogeneous sample of sources. Secondly, this distribution is strongly influenced by the *Planck* angular resolution (5′), therefore small (<1 pc) and compact clumps are likely local objects ($D < 1$ kpc), while larger objects (a few pc) are likely intrinsically extended structures located at large distances ($D > 1$ kpc). Hence, the double-peak pattern of the physical size distribution is strongly correlated with the distance distribution of Fig. 10, and is not likely to be a real feature.

6.3. Column density

The column density of the *Planck* cold clumps has been evaluated following the prescription in Planck Collaboration XXIII (2011),

$$N_{\rm H_2} = \frac{S'_\nu/\Omega}{\mu m_{\rm H} B_\nu(T)\,\kappa_\nu}, \quad (4)$$

where S'_ν is the flux density per beam at the frequency ν, which is integrated over the solid angle of the clump defined by $\Omega = \pi\theta_{\rm min}\theta_{\rm maj}/4$, $\mu = 2.33$ is the mean molecular weight, $m_{\rm H}$ is the mass of the atomic hydrogen, and κ_ν is the dust opacity. We have adopted the dust opacity from Beckwith et al. (1990), $\kappa_\nu = 0.1(\nu/1{\rm THz})^\beta\,{\rm cm^2\,g^{-1}}$, which is appropriate for the case of dense clouds at intermediate densities. The column density is computed at 857 GHz, close to the 1 THz reference of Beckwith et al. (1990), which allows us to minimize the impact of assuming a fixed emissivity spectral index, $\beta = 2$. Changing the emissivity spectral index in the range 1−3 yields up to 15% variations

on the emissivity estimate, which is negligible compared to the intrinsic uncertainty of the emissivity. This is also the *Planck*-HFI band where the S/N is the highest, and where dust emission remains optically thin. We note that S'_{857}, integrated over Ω, is half the flux density provided in the catalogue, S_{857}, which is the flux density integrated over the whole clump.

The peak column density is defined by

$$N_{\rm H_2}^{\rm peak} = \frac{I_\nu}{\mu m_{\rm H}\, B_\nu(T)\, \kappa_\nu}, \quad (5)$$

where I_ν is the surface brightness measured at the peak, and it can be derived from $N_{\rm H_2}$ by multiplying by 1.38. We stress that these two estimates of the column density are derived for the *Planck* clumps only after removal of the warm component, which is not what is typically found in the literature.

The $N_{\rm H_2}$ distribution is shown in Fig. 12. This ranges from 6.8×10^{18} to 1.2×10^{23} cm^{-2}, with a median of 3.4×10^{20} cm^{-2} and 6.3×10^{20} cm^{-2} for sources with FQ = 1 and 2, respectively.

Sources with FQ = 2 have slightly larger column densities, which is expected if these sources effectively correspond to colder and denser objects. About 80% of the sources have a column density between 1.4×10^{20} and 3.7×10^{21} cm^{-2}. We emphasize that these column densities are averaged over the size of the clump which, at the *Planck* resolution, is likely inducing a bias at low values because of beam dilution effects. Indeed, as shown in Planck Collaboration XXII (2011), the *Herschel* higher angular resolution observations of a sample of PGCC sources have revealed complex substructures, characterized by lower temperatures and higher densities than the parent clump.

6.4. Mass and mean density

For sources with a reliable distance estimate, the mass of the clump is given by

$$M = \frac{S_\nu D^2}{\kappa_\nu B_\nu(T)}, \quad (6)$$

where S_ν is the flux density measured at 857 GHz, integrated over the solid angle Ω defined in Sect. 6.3, D is the distance, κ_ν is the dust opacity defined in Sect. 6.3, and $B_\nu(T)$ is the Planck function for a dust temperature T.

The mass distribution shown in Fig. 12, ranges from a few 10^{-2} to almost 10^5 $M_\odot$, probing a large variety of objects, from cores to giant molecular clouds. We stress that this mass distribution, as the linear size distribution discussed in Sect. 6.2, is biased by our distance sample, which we know being highly heterogeneous (see Sect. 5). This becomes clear when we partition the mass distribution according to distance, in particular by separating sources located closer (dashed line) or further (dotted line) than 1 kpc from the Sun. Furthermore, except for less than 40% of the cases where the distance estimates are obtained from molecular complex association providing highly reliable estimates, the uncertainty on the computed mass is mainly dominated by the uncertainty on the distance, which is about two to three times larger than the uncertainties on the temperature and flux density involved in the calculation. Hence about 84% of sources have mass estimates with a S/N between 1 and 2, and 16% with a S/N above 2. We note also that we have almost reached the theoretical sensitivity limit of *Planck* to low-mass cold cores, as it has been derived in Sect. 4.2, which is about 0.03 $M_\odot$ for a cold source located at 100 pc and having a column density of 10^{20} cm^{-2}.

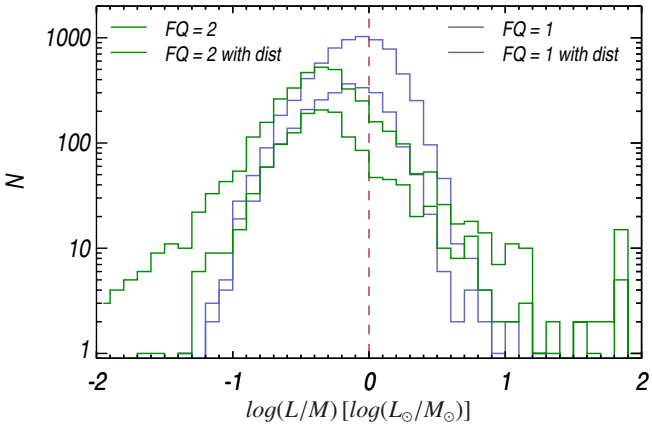

Fig. 13. Distribution of the luminosity to mass ratio of the PGCC clumps for sources with FQ = 1(blue line) and FQ = 2 (green line). The dot-dot-dot-dashed line denotes the distribution for the subsample of sources with a reliable distance estimate.

Finally, we have obtained the mean density of the clump, computed as $n_{\rm H_2} = M/V$, where V is the volume of the clump, modelled as a sphere of diameter equal to the physical size of the clump derived in Sect. 6.2. Figure 12 shows that the mean density ranges from 5.3 to 3.5×10^4 cm^{-3}, again spanning a wide range of object categories. While the smallest estimates are not consistent with typical density of large clouds (i.e., $\sim 10^2$ cm^{-3}, Williams et al. 2000; Blitz 1993), a closer look at the correlation with the size of the objects reveals that these values can be explained by a dilution effect in the *Planck* beam, as discussed in Sect. 6.6.

6.5. Luminosity

We have computed the bolometric luminosity of the cold clumps as

$$L = 4\pi D^2 \int_\nu S'_\nu {\rm d}\nu, \quad (7)$$

where D is the distance and S'_ν is the flux density of the clump modelled with a modified black body function with temperature T and emissivity spectral index β, as described in Sect. 6.1, and normalized to S_ν defined in Sect. 6.3. The integral is taken over the frequency range 300 GHz $< \nu <$ 10 THz, which extends beyond the IRAS and *Planck* spectral coverage. Any emission at shorter wavelengths is not included in this calculation. From Fig. 12 we note that the luminosity distributions for sources in the FQ = 1 and 2 categories are very heterogeneous, ranging from 10^{-2} to 10^6 $L_\odot$.

Figure 13 illustrates the L/M distribution. This quantity presents the advantage of not depending on distance, thus it can be derived for all the sources in the catalogue. It is often used as an indicator of the evolutionary stage of cold sources. About 73% and 83% of the sample with FQ = 1 and 2, respectively, have a $L/M < 1$, which is typical of objects with low degrees of evolution. Interestingly, we find the same proportion when we analyse the L/M distribution (dotted lines) for objects with a reliable distance estimate, suggesting that the sample of sources with distance estimates is statistically representative of the entire sample.

6.6. Correlation between physical properties

A summary of the statistical properties of the PGCC clod clumps physical quantities is provided in Table 6, for sources with

Table 6. Statistical description of the physical properties of the PGCC clumps with FQ = 1.

Percentile	T_c [K]	*FWHM* [′]	Size* [pc]	ε	N_{H_2} [cm^{-2}]	$D^\star$ [kpc]	$M^\star$ [$M_\odot$]	$n^\star_{H_2}$ [cm^{-3}]	$L^\star$ [$L_\odot$]
min.	8.6	3.4	0.14	0.10	6.8×10^{18}	0.07	5.1×10^{-2}	5.3×10^{0}	7.6×10^{-2}
first 1%	10.5	4.6	0.20	0.36	3.2×10^{19}	0.12	1.4×10^{-1}	1.6×10^{1}	1.4×10^{-1}
first 10% . . .	12.1	5.8	0.27	0.61	9.8×10^{19}	0.14	4.5×10^{-1}	6.8×10^{1}	3.6×10^{-1}
median	14.5	7.5	0.71	0.83	3.4×10^{20}	0.33	3.3×10^{0}	3.0×10^{2}	2.1×10^{0}
last 10%	17.0	9.3	1.91	0.94	1.8×10^{21}	0.92	5.9×10^{1}	2.4×10^{3}	6.9×10^{1}
last 1%	19.9	11.0	11.72	0.97	8.6×10^{21}	5.51	6.8×10^{3}	1.3×10^{4}	7.5×10^{3}
max.	30.0	13.1	25.16	0.98	8.8×10^{22}	10.48	2.6×10^{4}	3.5×10^{4}	7.6×10^{4}

Notes. The statistics of the quantities denoted with $^{(\star)}$ h as been computed on the subsample of sources having a distance estimate with `DIST_QUALITY`=1 or 2.

Table 7. Same as Table 6 with FQ = 2.

Percentile	T_c [K]	*FWHM* [′]	Size* [pc]	ε	N_{H_2} [cm^{-2}]	$D^\star$ [kpc]	$M^\star$ [$M_\odot$]	$n_{H_2}{}^\star$ [cm^{-3}]	$L^\star$ [$L_\odot$]
min.	5.8	2.8	0.15	0.16	1.4×10^{19}	0.07	5.0×10^{-2}	6.4×10^{0}	9.2×10^{-3}
first 1%	8.6	4.2	0.19	0.37	4.9×10^{19}	0.12	1.4×10^{-1}	1.4×10^{1}	6.4×10^{-2}
first 10% . . .	11.0	5.6	0.28	0.61	1.4×10^{20}	0.14	6.1×10^{-1}	6.4×10^{1}	2.7×10^{-1}
median	13.0	7.5	0.95	0.84	6.3×10^{20}	0.41	8.7×10^{0}	3.5×10^{2}	3.7×10^{0}
last 10%	15.7	9.7	8.55	0.95	3.7×10^{21}	4.38	3.1×10^{3}	2.6×10^{3}	3.3×10^{3}
last 1%	22.2	11.7	15.69	0.98	1.0×10^{22}	6.90	1.4×10^{4}	1.2×10^{4}	4.6×10^{4}
max.	30.0	14.5	30.56	0.98	1.2×10^{23}	10.16	6.3×10^{4}	2.4×10^{4}	2.9×10^{6}

Notes. The statistics of the quantities denoted with $^{(\star)}$ h as been computed on the subsample of sources having a distance estimate with `DIST_QUALITY`=1 or 2. We note that for this class of sources, we only provide an upper limit of the temperature.

FQ = 1, and in Table 7, for sources with FQ = 2. For each quantity the 1%, 10% lower and higher percentiles and the minimum, median and maximum values are reported. We stress that there is no systematic correlation between physical properties for the objects in the lowest and highest percentile bins. Indeed, the existence of a potential correlation between the physical properties of the clumps is explored in Fig. 14. Only sources with robust distance estimates (`DIST_QUALITY`=1 or 2) and reliable flux densities (`FLUX_QUALITY`=1 or 2) have been considered, amounting to a total of 3867 clumps. The locus of the Simon et al. (2006b) IRDCs properties is shown as red points, including local thermodynamic equilibrium (LTE) mass estimates.

As expected, the clumps size and mass are strongly correlated between them and with the distance estimate because of the FWHM of the PGCC sources which is mainly constrained by the 5′ *Planck* beam, ranging from 5.′6 to 9.′7 for 80% of the sources. Artefacts due to the distance association with molecular clouds are visible as straight lines in all the scatter plots including the distance. Comparing the PGCC distributions (black) to the IRDC population (red), it appears that the PGCC Galactic cold clumps correspond statistically to smaller objects located in the solar neighbourhood and detected at all latitudes, while the IRDCs are preferentially detected towards the Galactic plane and represent distant structures. Furthermore, IRDCs appear more massive and dense than the PGCC sources.

It is also interesting to notice that the population of PGCC at very low column density ($<10^{20}$ cm^2) corresponds to sources with an intermediate linear size, from 0.5 to 2 pc. This is fully consistent with the dilution of a dense core of 0.1 pc with a column density of 10^{22} cm^2 at a distance of 500 pc in the *Planck* beam (5′). Similarly, we can explain the very low density estimates (a few cm^{-3}), which are not expected even for large clouds.

7. Ancillary Validation

7.1. Identification with Planck internal catalogues

We have performed a positional cross-correlation of the PGCC catalogue with the other *Planck* internal catalogues, using a 5′ radius. In particular, we have considered: the Early Cold Cores catalogue (ECC), the *Planck* Catalogue of Compact Sources (PCCS), the *Planck* Catalogue of Sunyaev-Zeldovich sources (PSZ), and the *Planck* Catalogue of High-redshift source candidates (PH*z*). The results are summarized in Table 8.

7.1.1. ECC

The Early Cold Cores catalogue contains 915 sources that were detected with high S/N by the *Planck* Early Mission using the same colour-detection method used for the PGCC catalogue. We find matches in positions for 892 ECC sources. The missing 23 ECC sources have a strong signal in all three detection maps. However, we have deblended the detection maps using the local maxima of the detection signal (see Montier et al. 2010, Sect. 5.2), and adopted the positions of these local maxima for the coordinates of the detections at each frequency.

The individual frequency catalogues have then been merged to create the final catalogue. This last step of band merging has been improved in the final version of the catalogue to ensure a higher degree of compactness of the detected clump across the frequencies. The missing 23 ECC sources do no longer satisfy the compactness criterion. This does not mean that these ECC sources are spurious, rather it suggests that they are slightly more extended than the rest of the sources in the catalogue, hence they are discarded.

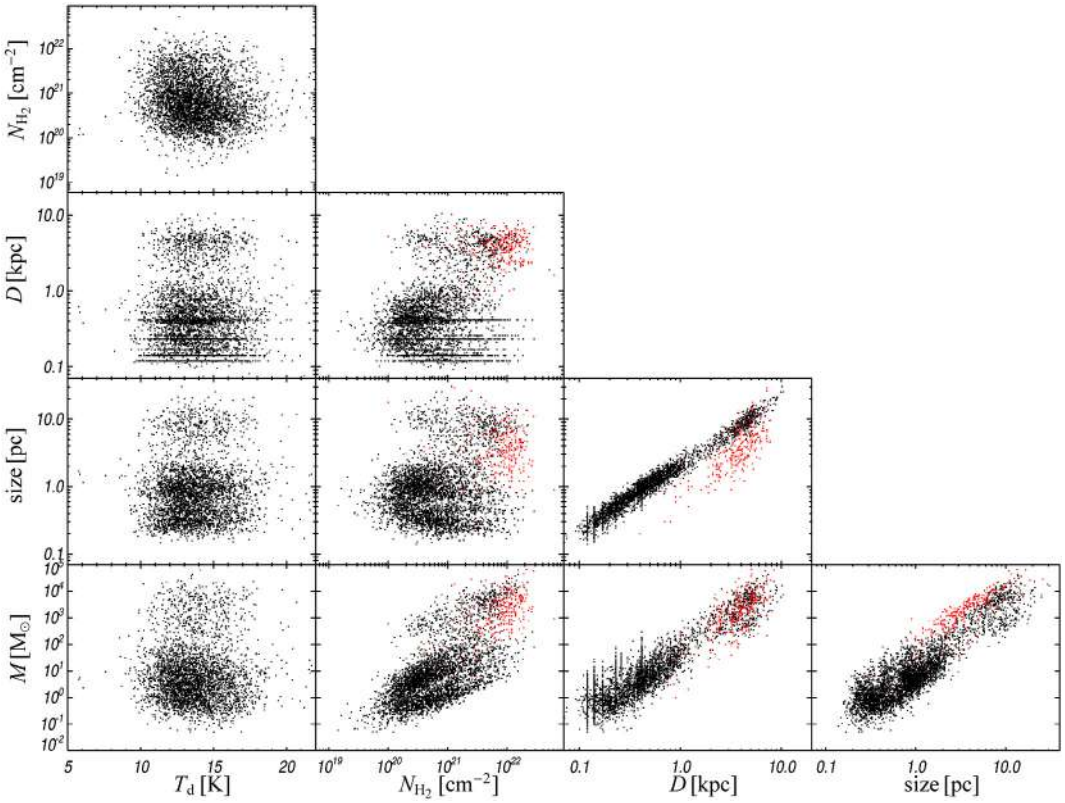

Fig. 14. Correlation plots for: temperature, column density, distance, size and mass. The black dots represent 3867 PGCC sources with a robust distance and flux density estimate. The red dots denote the IRDCs from Simon et al. (2006b).

7.1.2. PCCS

The PCCS (Planck Collaboration I 2016) contains frequency catalogues in each *Planck* band.The PCCS detections are obtained from individual frequency maps to which a Mexican Hat Wavelet filter has been applied. This procedure allows removal of extended emission and noise. Because of this data treatment, the S/N of PCCS sources depends on the frequency and on the area of the sky. The detections in each band are divided into two categories depending on the region of the sky: zone 0 corresponds to regions where the reliability of the sources has been quantified, while zones 1 to 3 correspond to filaments, Galactic regions or filaments in Galactic regions, respectively. The second category of PCCS sources is considered to have a lower reliability than the zone 0 sources.

The number of retrieved matches is given in Table 8. In the Table we provide the total number of matches (last column), as well as by `FLUX_QUALITY` flag (second, third and fourth columns). This is given for each subcategory of the PCCS catalogue: zone 0 and zones 1−3. Since the PCCS catalogue contains warm sources that are rejected from the PGCC catalogue, it is not surprising that we do not find PGCC matches for all the PCCS detections. However, an important fraction of the PGCC sources have a counterpart in the PCCS catalogue, especially in the highest frequency channels, up to 75% in the 857 GHz band when including the zones 1−3 sources. We also note that the proportion of matched sources in the low-frequency channels becomes extremely small (131 in total) and mainly consists of zone-0 sources, which could represent a population of extragalactic radio contaminants that has not been fully rejected. More interestingly, the PGCC detection algorithm requires a detection in all three frequency cold residual maps, while the PCCS only requires single frequency detections. There are 21 182 PCCS sources that are simultaneously detected at 857, 545, and 353 GHz. Of these, 7038 have a match in the PGCC catalogue in a 5′ radius. Thus the PGCC catalogue contains ∼45% of new sources not already identified in the PCCS catalogue in the three upper *Planck* frequencies as cold sources.

7.1.3. PSZ

The Planck Catalogue of Sunyaev-Zeldovich sources (PSZ, Planck Collaboration XXVIII 2016) contains 1653 detections. These are exclusively extragalactic sources, so the overlap between the PSZ and PGCC catalogues is small, i.e., 65 sources. Most of these sources exhibit cold temperature, except one which is warm. Since the `CoCoCoDeT` algorithm is suited to detect sources whose SED peaks around 857 GHz, it is not expected to be sensitive to the SZ effect from galaxy clusters, which is characterized by a peak at 353 GHz and almost no emission contribution at 857 GHz. Hence it is likely that this sample of 65 matched sources, lying at the limit of the Galactic mask used when building the PSZ catalogue, consists of Galactic cold clumps at intermediate to high latitudes, therefore representing a contaminant for the PSZ catalogue.

7.1.4. PHz

The Planck list of high-z source candidates (PHz, Planck Collaboration Int. XXXIX 2015) is a list of sources detected at high latitude, in the 26% cleanest fraction of the sky, and consists of a sample of high-redshift candidates identified by their "red" colours in the *Planck* highest frequency bands. By cross-correlating the PGCC and PHz catalogues, we found 15 common

Table 8. Result of the positional cross-correlation of the PGCC catalogue with the other *Planck* internal catalogues.

Catalogue	Option	N	PGCC FLUX_QUALITY 1 (6993)	2 (3755)	3 (2440)	Total (13 188)
ECC		915	622	237	55	892
PCCS 857	zone 0	4891	55	9	5	69
	zone 1–3	43 290	5361	2511	1725	9597
PCCS 545	zone 0	1694	67	15	12	94
	zone 1–3	31 068	5010	2412	1596	9018
PCCS 353	zone 0	1344	59	17	8	84
	zone 1–3	22 665	4645	2227	1393	8265
PCCS 217	zone 0	2135	168	15	27	210
	zone 1–3	16842	3963	1836	1129	6928
PCCS 143	zone 0	2160	106	12	9	127
	zone 1–3	4139	959	748	320	2027
PCCS 100	zone 0	1742	119	26	20	165
	zone 1–3	2487	545	478	225	1248
PCCS 70	zone 0	1101	17	23	14	54
	zone 1–3	195	6	8	6	20
PCCS 44	zone 0	830	6	17	13	36
	zone 1–3	104	–	5	1	6
PCCS 30	zone 0	1435	16	19	18	53
	zone 1–3	125	2	5	6	13
PCCS 857x545x357	zone 0	648	27	8	2	37
	zone 1–3	20 534	3946	1890	1165	7001
PSZ		1653	31	16	18	65
PHz		2151	2	13	–	15

sources. This result was partly expected, due to the similar spectral behaviour of Galactic cold objects and extragalactic red sources. Nevertheless, at the time of writing the nature of these matches is uncertain and requires further investigation.

7.2. Crosscheck with follow-up observations

7.2.1. *Herschel* imaging

A subsample of the PGCC sources has been further investigated in the *Herschel* open time key programme Galactic Cold Cores (hereafter, HKP-GCC). *Herschel* PACS and SPIRE instruments were used to observe 115 fields at five wavelengths, from 100 μm to 500 μm, with an angular resolution from 12″ to 37″. The fields were selected based on an early version of the PGCC catalogue, and target 349 individual *Planck* clumps, spanning a wide range in S/N, latitude and temperature.

The sensitivity and resolution of the *Herschel* instruments (Pilbratt et al. 2010; Poglitsch et al. 2010; Griffin et al. 2010) enable detailed studies of the structure of the clumps and their interplay with their parent clouds. First results of the *Herschel* follow-up have been presented in Juvela et al. (2010, 2011, 2012) and in Planck Collaboration XXII (2011).

For the purpose of target selection, the *Planck* cold clumps have been binned according to their Galactic coordinates, their estimated dust colour temperature, and their mass. The bins are identified by the following boundary values: l = 0, 60, 120, and 180 deg; $|b|$ = 1, 5, 10, and 90 deg; $T_{\rm dust}$ = 6, 9, 11, and 14 K; M = 0, 0.01, 2.0, 500, $10^6\,M_\odot$. Here $T_{\rm dust}$ is the clump cold dust temperature. After creating the bins, the targets have been selected using a Monte Carlo technique, in which we have uniformly sampled the sources in the various bins. This procedure allows us to cover entirely the parameter space, including sources at high latitudes and with extreme mass values. The M = 0 bin has been reserved for sources with no distance estimate.

Interestingly, the selection of the PGCC sources had to avoid areas of the sky covered by other *Herschel* Key Programmes, such as the Galactic plane for $|b| < 1°$, which was targeted by the Hi-GAL programme (Molinari et al. 2010), and several nearby clouds that are included in the Gould Belt (André et al. 2010) and HOBYS (e.g., Motte et al. 2010) programmes.

The final selection of 115 fields includes 16 fields at Galactic latitudes above 20 degrees. The median peak column density in these fields is $N_{\rm H_2} = 1.5 \times 10^{21}$ cm^{-2} (for details on the column density calculation see Juvela et al. 2012). In each follow-up field, the *Planck* clump coordinates clearly identify a coherent structure in the *Herschel* surface brightness maps. This is the case even when the surface brightness is below 5 MJy sr^{-1} at 250 μm, suggesting that the CoCoCoDeT algorithm is able to reliably extract very low column density features from the *Planck* data.

The *Herschel* data have been used to generate column density and colour temperature maps (Montillaud et al. 2015). Figure 15 shows the pixel-to-pixel two-dimensional distribution of column density vs. temperature. Pixels located within 1σ of the elliptical Gaussian fit of the PGCC sources are defined as IN pixels, and are shown with cyan contours in the figure. They exhibit a much narrower distribution with respect to pixels located outside the PGCC sources, defined as OUT pixels. The IN pixels are mostly found in correspondance of the coldest and

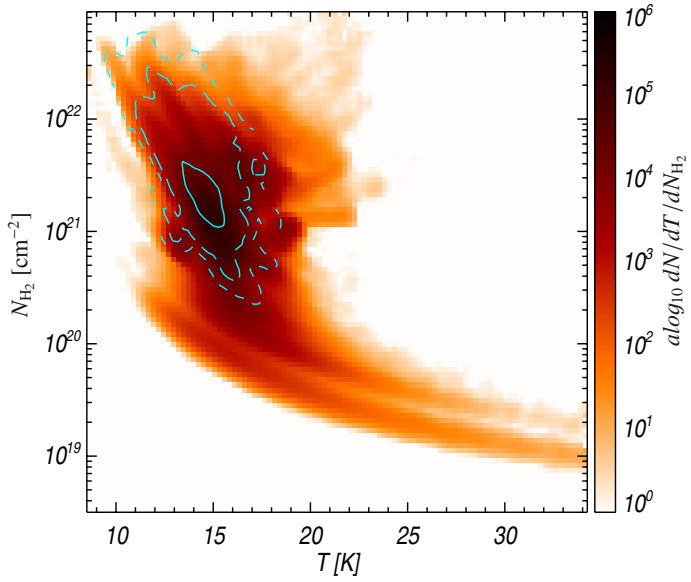

Fig. 15. Temperature vs. column density two-dimensional distribution for all PGCC cold clumps followed up by *Herschel* in the HKP-GCC programme. The plotted data points are identified as IN and OUT: IN points are located inside the *Planck* clump solid angle, while the OUT points are located outside. The distribution of the OUT points is shown in colour, while the distribution of the IN points is denoted by cyan contours at three different levels: 10, 50 and 90% of the maximum.

densest regions of the two-dimensional diagram, while the OUT pixels are also in regions of low column density and relatively high temperature. This result highlights the dense and cold nature of the PGCC sources. We note that the tail at high temperature and low column density is associated with pixels with low S/N pixels and reflects the ambiguity in the fitting and the functional dependence between the temperature and the column density in such conditions.

Based on the *Herschel* follow-up, Montillaud et al. (2015) have also built a catalogue of compact sources. After removing extragalactic contaminants, pre-stellar candidates have been identified with a multi-wavelength analysis. Montillaud et al. (2015) have performed a detailed analysis aimed at classifying the *Herschel* sources according to their evolutionary stage, i.e., from starless cores to Young Stellar Objects (YSO). For each *Herschel* field, the fraction of YSOs and starless sources falling inside the 3σ elliptical Gaussian contour of the PGCC clumps are derived, providing a unique information of the evolutionary stage of the PGCC clumps observed as a whole with *Planck*. A preliminary analysis of the YSO and starless populations in the *Herschel* fields around the 349 PGCC sources has already shown that *Planck* clumps contain a mixture of the two populations in various proportions: we find a number of *Planck* clumps with only one source that is a starless core ($f_{\rm starless} = 1$), or a YSO ($f_{\rm YSO} = 1$), but more often sources composed by a mixture of YSOs and starless cores with fractions ranging from 10% to 50%. Again this illustrates the variety of sources covered by the PGCC catalogue, probing the ISM in extremely various evolutionary stages.

7.2.2. Gas tracers

In order to characterize the gas content of the *Planck* cold clumps, several ground-based follow-ups of dense medium tracers have been performed.

Wu et al. (2012) carried out a large survey of the ^{12}CO, ^{13}CO and C^{18}O $J = 1 \rightarrow 0$ transition, targeting 674 ECC clumps with the 13.7 m telescope of the Purple Mountain Observatory. All the clumps (except for one) have ^{12}CO and ^{13}CO detections, and 68% of them have C^{18}O emission. The three line peak velocities are found to coincide, suggesting that the *Planck* clumps are quite cold and quiescent. The comparison between the derived excitation temperature and the dust temperature shows that dust and gas are well coupled in 95% of the clumps. Ten of the ECC clumps were also mapped, evidencing substructures, such as cores, and filamentary/elongated morphologies.

8. Conclusion

The highest frequency bands of the *Planck*-HFI instrument provide an extremely powerful tracer of Galactic cold dust. By combining data from the *Planck* three upper bands with IRAS 3 THz data, we have conducted a multi-frequency compact source detection, and generated the Planck Catalogue of Galactic Cold Clumps (PGCC). A first version of this catalogue was released in 2011, i.e., the Early Cold Core catalogue (ECC), together with the Early Release Compact Source Catalogue (ERCSC). At that time, 915 sources, selected for their low temperature and high S/N, were made publicly available to the astronomical community. With the present work, we are releasing the whole PGCC catalogue, containing 13188 Galactic sources and 54 cold sources located in the LMC and SMC.

We have applied the `CoCoCoDeT` algorithm (Montier et al. 2010) to the *Planck* 857, 545, and 353 GHz maps and to the IRAS 3 THz data. The combined use of these maps allow the separation of the cold and warm emission components, hence the identification of sources colder than their local environment. Through a dedicated analysis, we have removed all possible extragalactic contaminants. In particular, we have cross-correlated the PGCC catalogue with publicly available extragalactic catalogues, leading to the rejection of fewer than one hundred sources, mostly at high Galactic latitude. In parallel, we have also discarded detections, which have turned out to be contaminated by the presence of nearby hot sources. Interestingly, the final catalogue contains 54 sources located in the LMC and SMC. These sources have been kept in the catalogue because the proximity of these dwarf galaxies makes it possible to detect individual clouds with *Planck*.

The PGCC sources have been divided into three categories, depending on the quality of their flux density estimates. 6993 sources have accurate photometry in both the *Planck* and IRAS bands. These sources correspond to FQ = 1 and are the most reliable in the catalogue. A total of 3755 sources have accurate flux densities in the *Planck* bands but not in the IRAS 3 THz band. These sources correspond to FQ = 2, and are likely so cold that their emission at 3 THz falls below the IRAS detection limit. The last category comprises 2440 sources, and for these no accurate flux density has been measured in at least two bands. These sources correspond to FQ = 3 and might be intrinsically very faint or still deeply embedded. Despite the poor photometry, they are considered real detections.

We have combined seven independent methods to assign a distance estimate to 5574 sources. In the PGCC catalogue, for each source we quote all the available distances derived from the different methods, however, only the most reliable estimate is used to compute other source physical quantities such as mass and luminosity. Distance estimates from different methods have been compared and validated. Accordingly, we have assigned, to each clump, a `DIST_QUALITY` flag: 464 sources

have consistent distance estimates (DIST_QUALITY=1); 4191 sources have only one estimate (DIST_QUALITY=2); 255 have incompatible estimates (DIST_QUALITY=3); 664 sources have only distance upper limits (DIST_QUALITY=4). More detailed on this analysis can be found in the on-line version of the PGCC catalogue. The 4655 sources with an accurate distance estimate (DIST_QUALITY=1 or 2) are mainly located in the solar neighbourhood, with about 85% of sources at less than 1 kpc, and 91.4% within 3 kpc from the Sun.

We have obtained the temperature for 10748 sources, using a free (for sources with FQ = 1) or fixed ($\beta = 2$, for sources with FQ = 2) emissivity spectral index. The catalogue temperature distribution confirms that the PGCC clumps are not only colder than their local environment (as by construction of the catalogue) but, more importantly, that they are intrinsically cold sources, with a median between 13 and 14.5 K, depending on the quality of the flux density measurements. The minimum temperature of the sources in the catalogue is 5.8 K, reached for sources with FQ = 2. It is important to emphasize that this value is not a threshold artificially induced by our detection method, which in fact has been shown (through a MCQA analysis) to provide a 60% completeness level at temperatures as low as 6 K. Therefore, we can confidently state that, at least at the *Planck* angular resolution, no Galactic source is colder than 5.8 K. This is consistent with dust temperature lower limits predicted by radiative modelling of the infrared heating in dense and cold cores (see, e.g., Bernard et al. 1992; Evans et al. 2001; Zucconi et al. 2001) yielding to a dust temperature of about 6 K. This is also in agreement with dust temperature measurements obtained towards dense pre-stellar cores, for example: $6.7 < T_{\rm d} < 7.5$ K in L183 (Pagani et al. 2004, 2007); $8.2 < T_{\rm d} < 9.8$ K in B68 (Nielbock et al. 2012) and L1689B (Roy et al. 2014); $T_{\rm d} \simeq T_{\rm g} = 5.5$ K in the inner core of L1544 (Crapsi et al. 2007). While heating by cosmic rays has already been suggested to explain the dust temperature lower limit in very obscured medium (Galli & Padovani 2015), this work does not allow us to derive any solid probe of such an effect because of the dilution within the *Planck* 5′ beam.

From the flux densities, temperature and distance estimates, we have derived other physical properties of the PGCC clumps, namely: column density, physical size, mass, mean density and luminosity. The column density of the *Planck* clumps covers almost five orders of magnitude, reaching a value as low as 6.8×10^{18} cm^{-2}, which can be compared to the sensitivity limit (3×10^{21} cm^{-2}) of the *MSX* absorption measurements used to detect IRDCs (Peretto & Fuller 2010). Hence objects detected in emission by *Planck* with the CoCoCoDeT algorithm may not be detected in absorption by MSX, meaning that the *Planck* PGCC sources might represent a larger class of objects than the IRDCs, and might include less dense and/or more deeply embedded objects. Furthermore, the PGCC sources are characterized by a wide range of sizes and mean densities, which is indicative of a variety of astrophysical sources and evolutionary stages. The physical size of the catalogue sources ranges from 0.14 pc to 30.6 pc, i.e., from the typical size of a cold core to the one of a giant molecular cloud. Similarly the mean density spans four orders of magnitude, from 5.3 to 3.5×10^4 cm^{-3}, encompassing the three categories introduced by Williams et al. (2000), which are cores, clumps and clouds.

We emphasize that, although we have adopted the term *clump* to refer to the generic source in the PGCC catalogue, we are aware that, depending on the distance, some of these sources are in fact cores, either pre- or proto-stellar, while others are giant molecular clouds. The preliminary *Herschel* and gas tracers follow-ups have confirmed that the PGCC sources are indeed cold and dense environments, but have also shown that they often contain colder substructures (e.g., cores) and even warm components (e.g., YSOs). In the future, other follow-ups of this kind, as well as cross-correlations with already existing ancillary data sets (e.g., *Herschel*, WISE or AKARI), will become necessary to shed light on the exact nature of the *Planck* clumps.

We believe that the PGCC catalogue, covering the whole sky, hence probing wildly different environments, represents a real goldmine for investigations of the early phases of star formation. These include, but are not limited to: i) studies of the evolution from molecular clouds to cores and the influence of the local conditions; ii) analysis of the *extreme* cold sources, such as the most massive clumps or those located at relatively high latitude; iii) characterization of the dust emission law in dense regions and the role of the environment. All these topics will be discussed in forthcoming publications.

Acknowledgements. The Planck Collaboration acknowledges the support of: ESA; CNES and CNRS/INSU-IN2P3-INP (France); ASI, CNR, and INAF (Italy); NASA and DoE (USA); STFC and UKSA (UK); CSIC, MINECO, J.A., and RES (Spain); Tekes, AoF, and CSC (Finland); DLR and MPG (Germany); CSA (Canada); DTU Space (Denmark); SER/SSO (Switzerland); RCN (Norway); SFI (Ireland); FCT/MCTES (Portugal); ERC and PRACE (EU). A description of the Planck Collaboration and a list of its members, indicating which technical or scientific activities they have been involved in, can be found at http://www.cosmos.esa.int/web/planck/planck-collaboration

References

Andersson, B.-G., Wannier, P. G., & Morris, M. 1991, ApJ, 366, 464
André, P., Men'shchikov, A., Bontemps, S., et al. 2010, A&A, 518, L102
Beckwith, S. V. W., Sargent, A. I., Chini, R. S., & Guesten, R. 1990, AJ, 99, 924
Bennett, A. S. 1962, MNRAS, 68, 163
Bernard, J. P., Boulanger, F., Desert, F. X., & Puget, J. L. 1992, A&A, 263, 258
Berry, M., Ivezić, Ž., Sesar, B., et al. 2012, ApJ, 757, 166
Bertout, C., Robichon, N., & Arenou, F., 1999, A&A, 352, 574
Blitz, L. 1993, in Protostars and Planets III, eds. E. H. Levy, & J. I. Lunine, 125
Bontemps, S., André, P., Könyves, V., et al. 2010, A&A, 518, L85
Canny, J. 1986, IEEE Communications Letters, 679
Covey, K. R., Ivezić, Ž., Schlegel, D., et al. 2007, AJ, 134, 2398
Crapsi, A., Caselli, P., Walmsley, M. C., & Tafalla, M. 2007, A&A, 470, 221
Dame, T. M., Hartmann, D., & Thaddeus, P. 2001, ApJ, 547, 792
Djorgovski, S. G., Carvalho, R. R., Gal, R. R., et al. 2003, Bull. Astron. Soc. Brazil, 23, 197
Dreyer, J. L. E. 1888, MNRAS, 49, 1
Dreyer, J. L. E. 1895, MNRAS, 51, 185
Edge, D. O., Shakeshaft, J. R., McAdam, W. B., Baldwin, J. E., & Archer, S. 1959, MNRAS, 68, 37
Enoch, M. L., Glenn, J., Evans, II, N. J., et al. 2007, ApJ, 666, 982
Evans, II, N. J., Rawlings, J. M. C., Shirley, Y. L., & Mundy, L. G. 2001, ApJ, 557, 193
Foster, J. B., Stead, J. J., Benjamin, R. A., Hoare, M. G., & Jackson, J. M. 2012, ApJ, 751, 157
Fukui, Y., Kawamura, A., Minamidani, T., et al. 2008, ApJS, 178, 56
Galli, D., & Padovani, M. 2015, ArXiv e-prints [arXiv:1502.03380]
Gordon, K. D., Roman-Duval, J., Bot, C., et al. 2014, ApJ, 797, 85
Gower, J. F. R., Scott, P. F., & Wills, D. 1967, MNRAS, 71, 49
Griffin, M. J., Abergel, A., Abreu, A., et al. 2010, A&A, 518, L3
Hilditch, R. W., Howarth, I. D., & Harries, T. J., 2005, MNRAS, 357, 304
Jackson, J., Finn, S., Rathborne, J., Chambers, E., & Simon, R. 2008, ApJ, 680, 349
Jones, D. O., West, A. A., & Foster, J. B. 2011, AJ, 142, 44
Juvela, M., & Ysard, N. 2012, A&A, 541, A33
Juvela, M., Ristorcelli, I., Montier, L. A., et al. 2010, A&A, 518, L93
Juvela, M., Ristorcelli, I., Pelkonen, V.-M., et al. 2011, A&A, 527, A111
Juvela, M., Ristorcelli, I., Pagani, L., et al. 2012, A&A, 541, A12
Juvela, M., Montillaud, J., Ysard, N., & Lunttila, T. 2013, A&A, 556, A63
Loinard, L. 2013, in IAU Symp. 289, ed. R. de Grijs, 36
Lombardi, M. 2009, A&A, 493, 735

Marshall, D. J., Robin, A. C., Reylé, C., Schultheis, M., & Picaud, S. 2006, A&A, 453, 635
Marshall, D. J., Joncas, G., & Jones, A. P. 2009, ApJ, 706, 727
McGehee, P. M., West, A. A., Smith, J. A., Anderson, K. S. J., & Brinkmann, J. 2005, AJ, 130, 1752
Messier, C., & Niles, P. H. 1981, The Messier catalogue of Charles Messier
Miville-Deschênes, M., & Lagache, G. 2005, ApJS, 157, 302
Molinari, S., Swinyard, B., Bally, J., et al. 2010, A&A, 518, L100
Montier, L. A., Pelkonen, V., Juvela, M., Ristorcelli, I., & Marshall, D. J. 2010, A&A, 522, A83
Montillaud, D. P., Juvela, M., Rivera-Ingraham, A., et al. 2015, A&A, 584, A92
Motte, F., Zavagno, A., Bontemps, S., et al. 2010, A&A, 518, L77
Murdin, P., & Penston, M. V. 1977, MNRAS, 181, 657
Netterfield, C. B., Ade, P. A. R., Bock, J. J., et al. 2009, ApJ, 707, 1824
Neugebauer, G., Habing, H. J., van Duinen, R., et al. 1984, ApJ, 278, L1
Nielbock, M., Launhardt, R., Steinacker, J., et al. 2012, A&A, 547, A11
Pagani, L., Bacmann, A., Motte, F., et al. 2004, A&A, 417, 605
Pagani, L., Bacmann, A., Cabrit, S., & Vastel, C. 2007, A&A, 467, 179
Peretto, N., & Fuller, G. A. 2010, ApJ, 723, 555
Pilbratt, G. L., Riedinger, J. R., Passvogel, T., et al. 2010, A&A, 518, L1
Pilkington, J. D. H., & Scott, J. F. 1965, MNRAS, 69, 183
Poglitsch, A., Waelkens, C., Geis, N., et al. 2010, A&A, 518, L2
Planck Collaboration. 2011, The Explanatory Supplement to the Planck Early Release Compact Source Catalogue (ESA)
Planck Collaboration VII. 2011, A&A, 536, A7
Planck Collaboration XXII. 2011, A&A, 536, A22
Planck Collaboration XXIII. 2011, A&A, 536, A23
Planck Collaboration I. 2014, A&A, 571, A1
Planck Collaboration IV. 2014, A&A, 571, A4
Planck Collaboration VI. 2014, A&A, 571, A6
Planck Collaboration VII. 2014, A&A, 571, A7
Planck Collaboration VIII. 2014, A&A, 571, A8
Planck Collaboration IX. 2014, A&A, 571, A9
Planck Collaboration XIII. 2014, A&A, 571, A13
Planck Collaboration XXVIII. 2014, A&A, 571, A28
Planck Collaboration I. 2016, A&A, 594, A1
Planck Collaboration II. 2016, A&A, 594, A2
Planck Collaboration III. 2016, A&A, 594, A3
Planck Collaboration IV. 2016, A&A, 594, A4
Planck Collaboration V. 2016, A&A, 594, A5
Planck Collaboration VI. 2016, A&A, 594, A6
Planck Collaboration VII. 2016, A&A, 594, A7
Planck Collaboration VIII. 2016, A&A, 594, A8
Planck Collaboration IX. 2016, A&A, 594, A9
Planck Collaboration X. 2016, A&A, 594, A10
Planck Collaboration XI. 2016, A&A, 594, A11
Planck Collaboration XII. 2016, A&A, 594, A12
Planck Collaboration XIII. 2016, A&A, 594, A13
Planck Collaboration XIV. 2016, A&A, 594, A14
Planck Collaboration XV. 2016, A&A, 594, A15
Planck Collaboration XVI. 2016, A&A, 594, A16
Planck Collaboration XVII. 2016, A&A, 594, A17
Planck Collaboration XVIII. 2016, A&A, 594, A18
Planck Collaboration XIX. 2016, A&A, 594, A19
Planck Collaboration XX. 2016, A&A, 594, A20
Planck Collaboration XXI. 2016, A&A, 594, A21
Planck Collaboration XXII. 2016, A&A, 594, A22
Planck Collaboration XXIII. 2016, A&A, 594, A23
Planck Collaboration XXIV. 2016, A&A, 594, A24
Planck Collaboration XXV. 2016, A&A, 594, A25
Planck Collaboration XXVI. 2016, A&A, 594, A26
Planck Collaboration XXVII. 2016, A&A, 594, A27
Planck Collaboration XXVIII. 2016, A&A, 594, A28
Planck Collaboration Int. XXXIX. 2015, A&A, submitted [arXiv:1508.04171]
Robin, A., Reylé, C., Derrière, S., & Picaud, S. 2003, A&A, 409, 523
Robin, A. C., Reylé, C., Marshall, D. J., & Schultheis, M. 2012, The Besançon Model of Stellar Population Synthesis of the Galaxy, eds. A. Miglio, J. Montalbán, & A. Noels, 171
Roy, A., André, P., Palmeirim, P., et al. 2014, A&A, 562, A138
Russell, S. C., & Dopita, M. A. 1992, ApJ, 384, 508
Schlafly, E. F., Green, G., Finkbeiner, D. P., et al. 2014, ApJ, 786, 29
Shetty, R., Kauffmann, J., Schnee, S., & Goodman, A. A. 2009, ApJ, 696, 676
Simon, R., Jackson, J. M., Rathborne, J. M., & Chambers, E. T. 2006a, ApJ, 639, 227
Simon, R., Rathborne, J. M., Shah, R. Y., Jackson, J. M., & Chambers, E. T. 2006b, ApJ, 653, 1325
Skrutskie, M. F., Cutri, R. M., Stiening, R., et al. 2006, AJ, 131, 1163
Stanimirovic, S., Staveley-Smith, L., Dickey, J. M., Sault, R. J., & Snowden, S. L. 1999, MNRAS, 302, 417
Staveley-Smith, L., Kim, S., Calabretta, M. R., Haynes, R. F., & Kesteven, M. J. 2003, MNRAS, 339, 87
Walker, A. R. 2012, Ap&SS, 341, 43
Williams, J. P., Blitz, L., & McKee, C. F. 2000, in Protostars and Planets IV, eds. V. Mannings, A. P. Boss, & S. S. Russell (University of Arizona Press), 97
Wong, T., Hughes, A., Ott, J., et al. 2011, ApJS, 197, 16
Wu, Y., Liu, T., Meng, F., et al. 2012, ApJ, 756, 76
Ysard, N., Juvela, M., Demyk, K., et al. 2012, A&A, 542, A21
Zucconi, A., Walmsley, C. M., & Galli, D. 2001, A&A, 376, 650

[1] APC, AstroParticule et Cosmologie, Université Paris Diderot, CNRS/IN2P3, CEA/lrfu, Observatoire de Paris, Sorbonne Paris Cité, 10 rue Alice Domon et Léonie Duquet, 75205 Paris Cedex 13, France
[2] African Institute for Mathematical Sciences, 6−8 Melrose Road, Muizenberg, Cape Town, South Africa
[3] Agenzia Spaziale Italiana Science Data Center, via del Politecnico snc, 00133 Roma, Italy
[4] Aix-Marseille Université, CNRS, LAM (Laboratoire d'Astrophysique de Marseille) UMR 7326, 13388 Marseille, France
[5] Astrophysics Group, Cavendish Laboratory, University of Cambridge, J J Thomson Avenue, Cambridge CB3 0HE, UK
[6] Astrophysics & Cosmology Research Unit, School of Mathematics, Statistics & Computer Science, University of KwaZulu-Natal, Westville Campus, Private Bag X54001, 4000 Durban, South Africa
[7] CITA, University of Toronto, 60 St. George St., Toronto, ON M5S 3H8, Canada
[8] CNRS, IRAP, 9 Av. colonel Roche, BP 44346, 31028 Toulouse Cedex 4, France
[9] CRANN, Trinity College, Dublin, Ireland
[10] California Institute of Technology, Pasadena, California, USA
[11] Centre for Theoretical Cosmology, DAMTP, University of Cambridge, Wilberforce Road, Cambridge CB3 0WA, UK
[12] Centro de Estudios de Física del Cosmos de Aragón (CEFCA), Plaza San Juan, 1, planta 2, 44001 Teruel, Spain
[13] Computational Cosmology Center, Lawrence Berkeley National Laboratory, Berkeley, California, USA
[14] Consejo Superior de Investigaciones Científicas (CSIC), Madrid, Spain
[15] DSM/Irfu/SPP, CEA-Saclay, 91191 Gif-sur-Yvette Cedex, France
[16] DTU Space, National Space Institute, Technical University of Denmark, Elektrovej 327, 2800 Kgs. Lyngby, Denmark
[17] Département de Physique Théorique, Université de Genève, 24 quai E. Ansermet, 1211 Genève 4, Switzerland
[18] Departamento de Física, Universidad de Oviedo, Avda. Calvo Sotelo s/n, Oviedo, Spain
[19] Department of Astronomy and Astrophysics, University of Toronto, 50 Saint George Street, Toronto, Ontario, Canada
[20] Department of Astrophysics/IMAPP, Radboud University Nijmegen, PO Box 9010, 6500 GL Nijmegen, The Netherlands
[21] Department of Physics & Astronomy, University of British Columbia, 6224 Agricultural Road, Vancouver, British Columbia, Canada
[22] Department of Physics and Astronomy, Dana and David Dornsife College of Letter, Arts and Sciences, University of Southern California, Los Angeles, CA 90089, USA
[23] Department of Physics and Astronomy, University College London, London WC1E 6BT, UK
[24] Department of Physics, Florida State University, Keen Physics Building, 77 Chieftan Way, Tallahassee, Florida, USA
[25] Department of Physics, Gustaf Hällströmin katu 2a, University of Helsinki, 00100 Helsinki, Finland
[26] Department of Physics, Princeton University, Princeton, NJ 00185, USA
[27] Department of Physics, University of California, Santa Barbara, California, USA
[28] Department of Physics, University of Illinois at Urbana-Champaign, 1110 West Green Street, Urbana, Illinois, USA

[29] Dipartimento di Fisica e Astronomia G. Galilei, Università degli Studi di Padova, via Marzolo 8, 35131 Padova, Italy
[30] Dipartimento di Fisica e Scienze della Terra, Università di Ferrara, via Saragat 1, 44122 Ferrara, Italy
[31] Dipartimento di Fisica, Università La Sapienza, P.le A. Moro 2, Roma, Italy
[32] Dipartimento di Fisica, Università degli Studi di Milano, via Celoria, 16 Milano, Italy
[33] Dipartimento di Fisica, Università degli Studi di Trieste, via A. Valerio 2 Trieste, Italy
[34] Dipartimento di Fisica, Università di Roma Tor Vergata, via della Ricerca Scientifica, 1 Roma, Italy
[35] Dipartimento di Matematica, Università di Roma Tor Vergata, via della Ricerca Scientifica, 1 Roma, Italy
[36] Discovery Center, Niels Bohr Institute, Blegdamsvej 17 Copenhagen, Denmark
[37] Dpto. Astrofísica, Universidad de La Laguna (ULL), 38206 La Laguna, Tenerife, Spain
[38] European Space Agency, ESAC, Planck Science Office, Camino bajo del Castillo, s/n, Urbanización Villafranca del Castillo, Villanueva de la Cañada, 28692 Madrid, Spain
[39] European Space Agency, ESTEC, Keplerlaan 1, 2201 AZ Noordwijk, The Netherlands
[40] Facoltà di Ingegneria, Università degli Studi e-Campus, via Isimbardi 10, 22060 Novedrate (CO), Italy
[41] Gran Sasso Science Institute, INFN, viale F. Crispi 7, 67100 L'Aquila, Italy
[42] HGSFP and University of Heidelberg, Theoretical Physics Department, Philosophenweg 16, 69120 Heidelberg, Germany
[43] Helsinki Institute of Physics, Gustaf Hällströmin katu 2, University of Helsinki, Helsinki, Finland
[44] INAF−Osservatorio Astrofisico di Catania, via S. Sofia 78 Catania, Italy
[45] INAF−Osservatorio Astronomico di Padova, Vicolo dell'Osservatorio 5 Padova, Italy
[46] INAF−Osservatorio Astronomico di Roma, via di Frascati 33 Monte Porzio Catone, Italy
[47] INAF−Osservatorio Astronomico di Trieste, via G.B. Tiepolo 11,Trieste, Italy
[48] INAF/IASF Bologna, via Gobetti, 101 Bologna, Italy
[49] INAF/IASF Milano, via E. Bassini, 15 Milano, Italy
[50] INFN, Sezione di Bologna, via Irnerio 46, 40126 Bologna, Italy
[51] INFN, Sezione di Roma 1, Università di Roma Sapienza, Piazzale Aldo Moro 2, 00185 Roma, Italy
[52] INFN, Sezione di Roma 2, Università di Roma Tor Vergata, via della Ricerca Scientifica, 1 Roma, Italy
[53] INFN/National Institute for Nuclear Physics, via Valerio 2, 34127 Trieste, Italy
[54] IPAG: Institut de Planétologie et d'Astrophysique de Grenoble, Université Grenoble Alpes, IPAG; CNRS, IPAG, 38000 Grenoble, France
[55] IUCAA, Post Bag 4, Ganeshkhind, Pune University Campus, 411 007 Pune, India
[56] Imperial College London, Astrophysics group, Blackett Laboratory, Prince Consort Road, London, SW7 2AZ, UK
[57] Infrared Processing and Analysis Center, California Institute of Technology, Pasadena, CA 91125 USA
[58] Institut Néel, CNRS, Université Joseph Fourier Grenoble I, 25 rue des Martyrs, Grenoble, France
[59] Institut Universitaire de France, 103 bd Saint-Michel, 75005 Paris, France
[60] Institut d'Astrophysique Spatiale, CNRS (UMR 8617) Université Paris-Sud 11, Bâtiment 121, Orsay, France
[61] Institut d'Astrophysique de Paris, CNRS (UMR 7095), 98bis boulevard Arago, 75014 Paris, France
[62] Institute of Astronomy, University of Cambridge, Madingley Road, Cambridge CB3 0HA, UK
[63] Institute of Theoretical Astrophysics, University of Oslo, Blindern, 0371 Oslo, Norway
[64] Instituto de Astrofísica de Canarias, C/Vía Láctea s/n, La Laguna, 38205 Tenerife, Spain
[65] Instituto de Física de Cantabria (CSIC-Universidad de Cantabria), Avda. de los Castros s/n, Santander, Spain
[66] Istituto Nazionale di Fisica Nucleare, Sezione di Padova, via Marzolo 8, 35131 Padova, Italy
[67] Jet Propulsion Laboratory, California Institute of Technology, 4800 Oak Grove Drive, Pasadena, California, USA
[68] Jodrell Bank Centre for Astrophysics, Alan Turing Building, School of Physics and Astronomy, The University of Manchester, Oxford Road, Manchester, M13 9PL, UK
[69] Kavli Institute for Cosmology Cambridge, Madingley Road, Cambridge, CB3 0HA, UK
[70] LAL, Université Paris-Sud, CNRS/IN2P3, Orsay, France
[71] LAPTh, Univ. de Savoie, CNRS, BP 110, 74941 Annecy-le-Vieux, France
[72] LERMA, CNRS, Observatoire de Paris, 61 avenue de l'Observatoire, Paris, France
[73] Laboratoire AIM, IRFU/Service d'Astrophysique – CEA/DSM – CNRS – Université Paris Diderot, Bât. 709, CEA-Saclay, 91191 Gif-sur-Yvette Cedex, France
[74] Laboratoire de Physique Subatomique et Cosmologie, Université Grenoble-Alpes, CNRS/IN2P3, 53 rue des Martyrs, 38026 Grenoble Cedex, France
[75] Laboratoire de Physique Théorique, Université Paris-Sud 11 and CNRS, Bâtiment 210, 91405 Orsay, France
[76] Lawrence Berkeley National Laboratory, Berkeley, CA 94720, USA
[77] Lebedev Physical Institute of the Russian Academy of Sciences, Astro Space Centre, 84/32 Profsoyuznaya st., Moscow, 117997 GSP-7, Russia
[78] Max-Planck-Institut für Astrophysik, Karl-Schwarzschild-Str. 1, 85741 Garching, Germany
[79] McGill Physics, Ernest Rutherford Physics Building, McGill University, 3600 rue University, Montréal, QC, H3A 2T8, Canada
[80] National University of Ireland, Department of Experimental Physics, Maynooth, Co. Kildare, Ireland
[81] Niels Bohr Institute, Blegdamsvej 17, Copenhagen, Denmark
[82] Optical Science Laboratory, University College London, Gower Street, London, UK
[83] SB-ITP-LPPC, EPFL, 1015 Lausanne, Switzerland
[84] SISSA, Astrophysics Sector, via Bonomea 265, 34136 Trieste, Italy
[85] School of Physics and Astronomy, Cardiff University, Queens Buildings, The Parade, Cardiff, CF24 3AA, UK
[86] School of Physics and Astronomy, University of Nottingham, Nottingham NG7 2RD, UK
[87] Sorbonne Université-UPMC, UMR7095, Institut d'Astrophysique de Paris, 98bis boulevard Arago, 75014 Paris, France
[88] Space Research Institute (IKI), Russian Academy of Sciences, Profsoyuznaya Str, 84/32, 117997 Moscow, Russia
[89] Space Sciences Laboratory, University of California, Berkeley, CA 94720, USA
[90] Special Astrophysical Observatory, Russian Academy of Sciences, Nizhnij Arkhyz, Zelenchukskiy region, 369167 Karachai-Cherkessian Republic, Russia
[91] Sub-Department of Astrophysics, University of Oxford, Keble Road, Oxford OX1 3RH, UK
[92] Theory Division, PH-TH, CERN, 1211 Geneva 23, Switzerland
[93] UPMC Univ Paris 06, UMR 7095, 98bis boulevard Arago, 75014 Paris, France
[94] Université de Toulouse, UPS-OMP, IRAP, 31028 Toulouse Cedex 4, France
[95] Universities Space Research Association, Stratospheric Observatory for Infrared Astronomy, MS 232-11, Moffett Field, CA 94035, USA
[96] University of Granada, Departamento de Física Teórica y del Cosmos, Facultad de Ciencias, 18071 Granada, Spain
[97] University of Granada, Instituto Carlos I de Física Teórica y Computacional, Granada, Spain
[98] Warsaw University Observatory, Aleje Ujazdowskie 4, 00-478 Warszawa, Poland

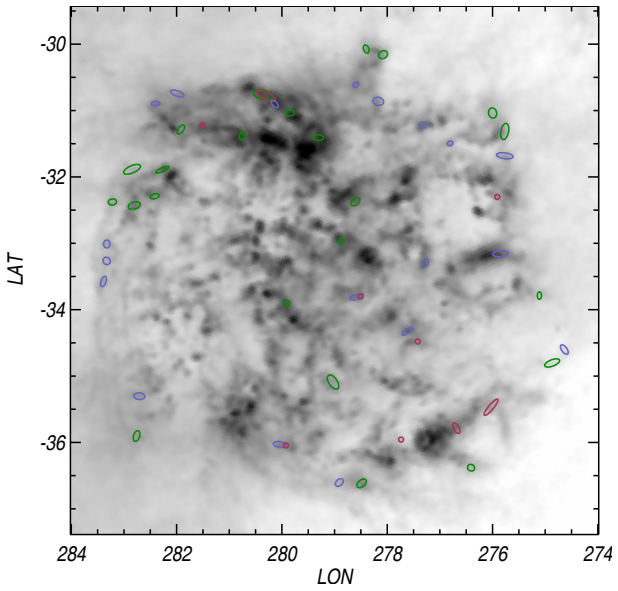

Fig. A.1. Distribution of the PGCC sources located in the LMC (in Galactic coordinates) for each `FLUX_QUALITY` category: "Reliable flux densities" (1, blue), "Missing 3 THz flux density" (2, green) and "Detection only" (3, pink). The grey scale image is the *Planck* intensity map at 857 GHz shown in log scale between 10^{-2} and 0.5 MJy sr^{-1}.

Appendix A: LMC – SMC

As noted in Sect. 3.3, the PGCC catalogue includes 51 sources located within a 4.°09 radius of the Large Magellanic Cloud (LMC), and three sources within a 2.°38 field centred on the Small Magellanic Cloud (SMC). Of the 51 sources in the LMC, 42 sources have FQ = 1 or 2, while 9 are considered only poor detections. In the SMC, two sources have a good `FLUX_QUALITY` flag and only one is detected.

At the distance of the Magellanic Clouds ($D_{\rm LMC}$ = 50.1 kpc, $D_{\rm SMC}$ = 61.7 kpc, Walker 2012; Hilditch et al. 2005), the working resolution of the *Planck* and IRAS maps (5′) corresponds to spatial scales of ∼80 pc, which is comparable to the characteristic size of giant molecular clouds (GMCs) in the Milky Way (∼50 pc, e.g., Blitz 1993). Magellanic PGCC sources are therefore quite different objects to Galactic PGCC sources, but they are still of considerable interest for studying the early phases of star formation. Firstly, the *Planck* data provide a census of cold material in the vicinity of the Magellanic Clouds that is independent of previous observations of HI and CO emission, the standard tracers of neutral interstellar gas in external galaxies. Secondly, PGCC sources in the Magellanic Clouds constitute a useful comparison sample to local GMCs with low levels of star formation, since the galactic environment hosting the cold molecular material is quite distinct. The clouds span a small but appreciable range of subsolar metallicities (0.2 to 0.5, Russell & Dopita 1992), and have dust-to-gas mass ratios that are ∼3 to 10 times lower than the value in the solar neighborhood (Gordon et al. 2014). They are also low-mass systems, with shallower gravitational potentials and lower levels of shear than the normal disc galaxies.

Of the 51 PGCC sources detected towards the LMC, 34 are located within the field surveyed by NANTEN at 2.′6 resolution for CO emission in the LMC (Fukui et al. 2008), while 27 sources are located inside the region observed by the higher resolution (45″) MAGMA LMC survey (Wong et al. 2011). All of these 27 sources exhibit CO emission that is well-detected by MAGMA, with peak integrated ^{12}CO $J = 1 \rightarrow 0$ intensities brighter than MAGMA's 4σ sensitivity limit (∼1.2 K km s^{-1}). Dedicated follow-up observations of the remaining Magellanic PGCC sources with the Mopra Telescope have detected CO emission associated with a further 15 PGCC sources in the LMC, but none of the three SMC sources (Hughes, in prep.). Figure A.1 shows the spatial distribution of all PGCC sources in the Magellanic Clouds. The spatial distribution of PGCC sources in the LMC is clearly not random: only one PGCC source is detected at high stellar surface densities ($\Sigma_* > 100\,{\rm Mpc}^2$) even though many CO clouds are detected there, while there are four PGCC sources that appear to be aligned in an east-west direction along the southern periphery of the LMC. These sources were previously noted in the dust property maps obtained by combining the IRAS and the *Planck* data as regions of low temperature and high dust column density.

In the LMC, the `CoCoCoDeT` algorithm therefore seems to be an efficient tool for identifying cold molecular material. After re-scaling for the lower dust-to-gas ratio in the LMC and accounting for mismatches between the intrinsic source size and the *Planck* and Mopra beam widths, the catalogued masses of the LMC PGCC sources are in good agreement with the masses derived from the Mopra CO data. A more detailed investigation of the spatial distribution and physical nature of the LMC PGCC sources will be presented in Hughes (in prep.).

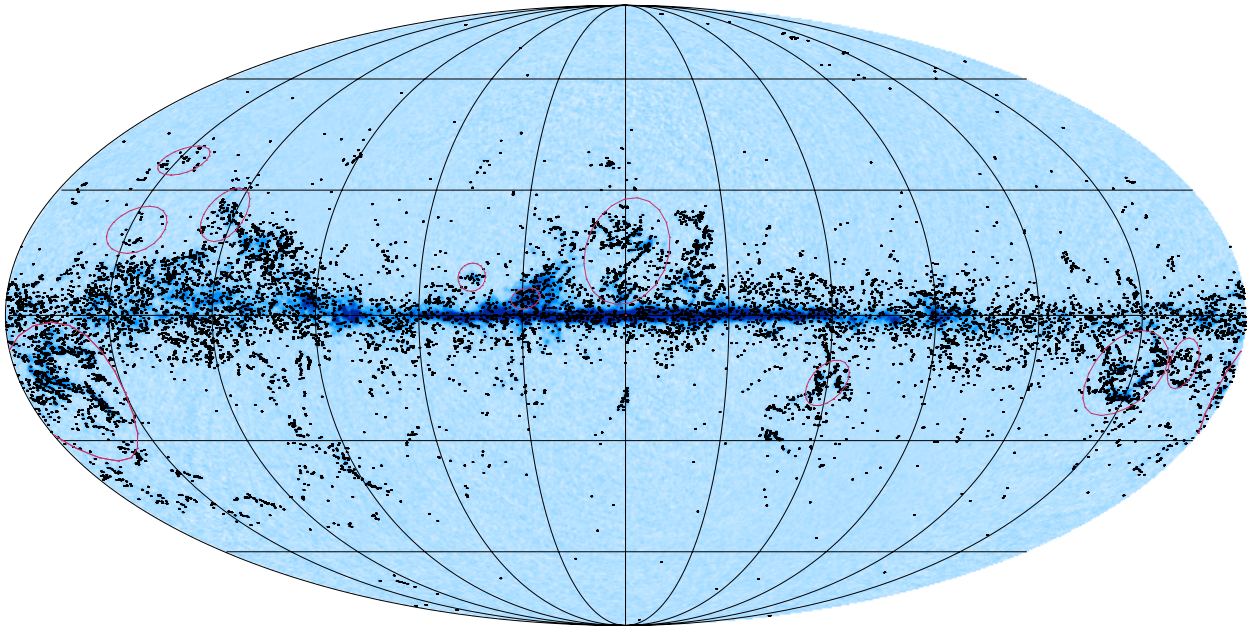

Fig. B.1. All-sky distribution of the PGCC sources with FQ = 1 or 2, displayed over the *Planck* ^{12}CO $J = 1 \rightarrow 0$ map ranging from −5 to 30 K kms^{-1}. The locations of the molecular complexes used in the distance estimate procedure are shown as red circles.

Appendix B: Correlation with CO map

In Fig. B.1 we overlay the all-sky distribution of the PGCC Galactic clumps to the *Planck* ^{12}CO $J = 1 \rightarrow 0$ all-sky map (see Planck Collaboration XIII 2014). As expected, for a large majority of the PGCC sources, their location coincides with a ^{12}CO $J = 1 \rightarrow 0$ transition. This is especially true in the Galactic disc. At high latitude, objects appear less associated with a CO signature, although this is likely due to the limited sensitivity of the *Planck* CO map. A further analysis is required to investigate whether the PGCC sources are associated with CO clumps, or only with diffuse CO emission.

Appendix C: Catalogue content

We detail in Table C.1 the content of the PGCC catalogue with a short description of each keyword. This information is also available and maintained up-to-date in the Planck Explanatory Supplement available at the following address: http://wiki.cosmos.esa.int/planckpla/index.php/Main_Page

Table C.1. PGCC catalogue columns.

Column name	Unit	Description
		Identification
NAME		Source name
SNR		Maximum S/N over the 857, 545, and 353 GHz *Planck* cold residual maps
SNR_857		S/N of the cold residual detection at 857 GHz
SNR_545		S/N of the cold residual detection at 545 GHz
SNR_353		S/N of the cold residual detection at 353 GHz
		Source position
GLON	[deg]	Galactic longitude based on morphology fitting
GLAT	[deg]	Galactic latitude (deg) based on morphology fitting
RA	[deg]	Right ascension (J2000) in degrees transformed from (GLON, GLAT)
DEC	[deg]	Declination (J2000) in degrees transformed from (GLON, GLAT)
		Morphology
GAU_MAJOR_AXIS	[arcmin]	FWHM along the major axis of the elliptical Gaussian
GAU_MAJOR_AXIS_SIG	[arcmin]	1σ uncertainty on the FWHM along the major axis
GAU_MINOR_AXIS	[arcmin]	FWHM along the minor axis of the elliptical Gaussian
GAU_MINOR_AXIS_SIG	[arcmin]	1σ uncertainty on the FWHM along the minor axis
GAU_POSITION_ANGLE	[rd]	Position angle of the elliptical Gaussian, defined as the clockwise angle between the Galactic plane orientation and the orientation of the major axis
GAU_POSITION_ANGLE_SIG	[rd]	1σ uncertainty on the position angle
		Photometry
FLUX_3000_CLUMP	[Jy]	Flux density of the clump at 3 THz
FLUX_3000_CLUMP_SIG	[Jy]	1σ uncertainty on the flux density of the clump at 3 THz
FLUX_857_CLUMP	[Jy]	Flux density of the clump at 857 GHz
FLUX_857_CLUMP_SIG	[Jy]	1σ uncertainty on the flux density of the clump at 857 GHz
FLUX_545_CLUMP	[Jy]	Flux density of the clump at 545 GHz
FLUX_545_CLUMP_SIG	[Jy]	1σ uncertainty on the flux density of the clump at 545 GHz
FLUX_353_CLUMP	[Jy]	Flux density of the clump at 353 GHz
FLUX_353_CLUMP_SIG	[Jy]	1σ uncertainty on the flux density of the clump at 353 GHz
FLUX_3000_WBKG	[Jy]	Flux density of the warm background at 3 THz
FLUX_3000_WBKG_SIG	[Jy]	1σ uncertainty on the flux density of the warm background at 3 THz
FLUX_857_WBKG	[Jy]	Flux density of the warm background at 857 GHz
FLUX_857_WBKG_SIG	[Jy]	1σ uncertainty on the flux density of the warm background at 857 GHz
FLUX_545_WBKG	[Jy]	Flux density of the warm background at 545 GHz
FLUX_545_WBKG_SIG	[Jy]	1σ uncertainty on the flux density of the warm background at 545 GHz
FLUX_353_WBKG	[Jy]	Flux density of the warm background at 353 GHz
FLUX_353_WBKG_SIG	[Jy]	1σ uncertainty on the flux density of the warm background at 353 GHz
FLUX_QUALITY	[1−3]	Category of flux density reliability
FLUX_BLENDING	[0, 1]	1 if blending issue with flux density estimate
FLUX_BLENDING_IDX		Catalogue index of the closest source responsible for blending
FLUX_BLENDING_ANG_DIST	[arcmin]	Angular distance to the closest source responsible for blending
FLUX_BLENDING_BIAS_3000	[%]	Relative bias of the flux density at 3 THz due to blending
FLUX_BLENDING_BIAS_857	[%]	Relative bias of the flux density at 857 GHz due to blending
FLUX_BLENDING_BIAS_545	[%]	Relative bias of the flux density at 545 GHz due to blending
FLUX_BLENDING_BIAS_353	[%]	Relative bias of the flux density at 353 GHz due to blending
		Distance
DIST_KINEMATIC	[kpc]	Distance estimate [1] using kinematics
DIST_KINEMATIC_SIG	[kpc]	1σ distance estimate using kinematics
DIST_OPT_EXT_DR7	[kpc]	Distance estimate [2] using optical extinction on SDSS DR7
DIST_OPT_EXT_DR7_SIG	[kpc]	1σ distance estimate using optical extinction on SDSS DR7
DIST_OPT_EXT_DR9	[kpc]	Distance estimate [3] using optical extinction on SDDS DR9
DIST_OPT_EXT_DR9_SIG	[kpc]	1σ distance estimate using optical extinction on SDSS DR9
DIST_NIR_EXT_IRDC	[kpc]	Distance estimate [4] using near-infrared extinction towards IRDCs
DIST_NIR_EXT_IRDC_SIG	[kpc]	1σ distance estimate using near-infrared extinction towards IRDCs
DIST_NIR_EXT	[kpc]	Distance estimate [5] using near-infrared extinction
DIST_NIR_EXT_SIG	[kpc]	1σ distance estimate using near-infrared extinction
DIST_MOLECULAR_COMPLEX	[kpc]	Distance estimate [6] using molecular complex association
DIST_MOLECULAR_COMPLEX_SIG	[kpc]	1σ distance estimate using molecular complex association
DIST_HKP_GCC	[kpc]	Distance estimate [7] from the *Herschel* key-programme Galactic cold cores
DIST_HKP_GCC_SIG	[kpc]	1σ distance estimate from the *Herschel* HKP-GCC
DIST_OPTION	[0−7]	Option of the best distance estimate used in other physical properties
DIST_QUALITY	[0−4]	Quality Flag of the consistency between distance estimates
DIST	[kpc]	Best distance estimate used for further physical properties
DIST_SIG	[kpc]	1σ uncertainty on the best distance estimate

Table C.1. continued.

Column name	Unit	Description
		Temperature
TEMP_CLUMP	[K]	Temperature of the clump with β as a free parameter
TEMP_CLUMP_SIG	[K]	1σ uncertainty on the clump temperature with β free
TEMP_CLUMP_LOW1	[K]	Lower 68% confidence limit of the clump temperature with β free
TEMP_CLUMP_UP1	[K]	Upper 68% confidence limit of the clump temperature with β free
BETA_CLUMP		Spectral index β of the clump
BETA_CLUMP_SIG		1σ uncertainty (from MCMC) on the emissivity spectral index β of the clump
BETA_CLUMP_LOW1		Lower 68% confidence limit of the emissivity spectral index β of the clump
BETA_CLUMP_UP1		Upper 68% confidence limit of the emissivity spectral index β of the clump
TEMP_BETA2_CLUMP	[K]	Temperature of the clump with $\beta = 2$
TEMP_BETA2_CLUMP_SIG	[K]	1σ uncertainty on the temperature of the clump with $\beta = 2$
TEMP_BETA2_CLUMP_LOW1	[K]	Lower 68% confidence limit of the clump temperature with $\beta = 2$
TEMP_BETA2_CLUMP_UP1	[K]	Upper 68% confidence limit of the clump temperature with $\beta = 2$
TEMP_WBKG	[K]	Temperature of the warm background with β as a free parameter
TEMP_WBKG_SIG	[K]	1σ uncertainty on the temperature of the warm background with β as a free parameter
TEMP_WBKG_LOW1	[K]	Lower 68% confidence limit of the warm background temperature with β free
TEMP_WBKG_UP1	[K]	Upper 68% confidence limit of the warm background temperature with β free
BETA_WBKG		Spectral index β of the warm background
BETA_WBKG_SIG		1σ uncertainty on the spectral index β of the warm background
BETA_WBKG_LOW1		Lower 68% confidence limit of the emissivity spectral index β of the warm background
BETA_WBKG_UP1		Upper 68% confidence limit of the emissivity spectral index β of the warm background
TEMP_BETA2_WBKG	[K]	Temperature of the warm background with $\beta = 2$
TEMP_BETA2_WBKG_SIG	[K]	1σ uncertainty on the temperature of the warm background with $\beta = 2$
TEMP_BETA2_WBKG_LOW1	[K]	Lower 68% confidence limit of the warm background temperature with $\beta = 2$
TEMP_BETA2_WBKG_UP1	[K]	Upper 68% confidence limit of the warm background temperature with $\beta = 2$
		Physical properties
NH2	[cm^{-2}]	Column density N_{H_2} of the clump
NH2_SIG	[cm^{-2}]	1σ uncertainty on the column density of the clump
NH2_LOW[1,2,3]	[cm^{-2}]	Lower 68%, 95% and 99% confidence limit of the column density
NH2_UP[1,2,3]	[cm^{-2}]	Upper 68%, 95% and 99% confidence limit of the column density
MASS	[$M_\odot$]	Mass estimate of the clump
MASS_SIG	[$M_\odot$]	1σ uncertainty on the mass estimate of the clump
MASS_LOW[1,2,3]	[$M_\odot$]	Lower 68%, 95% and 99% confidence limit of the mass estimate
MASS_UP[1,2,3]	[$M_\odot$]	Upper 68%, 95% and 99% confidence limit of the mass estimate
DENSITY	[cm^{-3}]	Mean density of the clump
DENSITY_SIG	[cm^{-3}]	1σ uncertainty on the mean density estimate of the clump
DENSITY_LOW[1,2,3]	[cm^{-3}]	Lower 68%, 95% and 99% confidence limit of the mean density estimate
DENSITY_UP[1,2,3]	[cm^{-3}]	Upper 68%, 95% and 99% confidence limit of the mean density estimate
SIZE	[pc]	Physical size of the clump
SIZE_SIG	[pc]	1σ uncertainty on the physical size estimate of the clump
SIZE_LOW[1,2,3]	[pc]	Lower 68%, 95% and 99% confidence limit of the physical size estimate
SIZE_UP[1,2,3]	[pc]	Upper 68%, 95% and 99% confidence limit of the physical size estimate
LUMINOSITY	[$L_\odot$]	Luminosity of the clump
LUMINOSITY_SIG	[$L_\odot$]	1σ uncertainty on the luminosity of the clump
LUMINOSITY_LOW[1, 2, 3]	[$L_\odot$]	Lower 68%, 95% and 99% confidence limit of the luminosity
LUMINOSITY_UP[1, 2, 3]	[$L_\odot$]	Upper 68%, 95% and 99% confidence limit of the luminosity
		Flags
NEARBY_HOT_SOURCE	[arcmin]	Distance to the closest hot source
XFLAG_LMC	[0, 1]	1 if part of the LMC
XFLAG_SMC	[0, 1]	1 if part of the SMC
XFLAG_ECC	[0, 1]	1 if present in the ECC
XFLAG_PCCS_857	[0, 1]	1 if present in the PCCS 857 GHz band
XFLAG_PCCS_545	[0, 1]	1 if present in the PCCS 545 GHz band
XFLAG_PCCS_353	[0, 1]	1 if present in the PCCS 353 GHz band
XFLAG_PCCS_217	[0, 1]	1 if present in the PCCS 217 GHz band
XFLAG_PCCS_143	[0, 1]	1 if present in the PCCS 143 GHz band
XFLAG_PCCS_100	[0, 1]	1 if present in the PCCS 100 GHz band
XFLAG_PCCS_70	[0, 1]	1 if present in the PCCS 70 GHz band
XFLAG_PCCS_44	[0, 1]	1 if present in the PCCS 44 GHz band
XFLAG_PCCS_30	[0, 1]	1 if present in the PCCS 30 GHz band
XFLAG_PSZ	[0,1]	1 if present in the PSZ
XFLAG_PHZ	[0,1]	1 if present in the PHZ
XFLAG_HKP_GCC	[0, 1]	1 if present in the *Herschel* HKP-GCC